

Rapid alkalinization factor 22 has a structural and signalling role in root hair cell wall assembly

Sébastjen Schoenaers, Hyun Kyung Lee, Martine Gonneau, Elvina Faucher, Thomas Levasseur, Elodie Akary, Naomi Claeijs, Steven Moussu, Caroline Broyart, Daria Balcerowicz, et al.

▶ To cite this version:

Sébastjen Schoenaers, Hyun Kyung Lee, Martine Gonneau, Elvina Faucher, Thomas Levasseur, et al.. Rapid alkalinization factor 22 has a structural and signalling role in root hair cell wall assembly. Nature Plants, 2024, 10.1038/s41477-024-01637-8. hal-04500803

HAL Id: hal-04500803

https://hal.science/hal-04500803

Submitted on 12 Mar 2024

HAL is a multi-disciplinary open access archive for the deposit and dissemination of scientific research documents, whether they are published or not. The documents may come from teaching and research institutions in France or abroad, or from public or private research centers.

L'archive ouverte pluridisciplinaire **HAL**, est destinée au dépôt et à la diffusion de documents scientifiques de niveau recherche, publiés ou non, émanant des établissements d'enseignement et de recherche français ou étrangers, des laboratoires publics ou privés.

A pectin-binding peptide with a structural and signaling role in the

2 assembly of the plant cell wall

- 3 Sébastjen Schoenaers^{1,2}, Hyun Kyung Lee³, Martine Gonneau², Elvina Faucher², Thomas Levasseur⁴,
- 4 Elodie Akary², Naomi Claeijs¹, Steven Moussu³, Caroline Broyart³, Daria Balcerowicz¹, Hamada
- 5 AbdElgawad¹, Andrea Bassi⁵, Daniel Santa Cruz Damineli^{6,7}, Alex Costa^{8,9}, José A Feijó⁶, Celine
- 6 Moreau⁴, Estelle Bonnin⁴, Bernard Cathala⁴, Julia Santiago^{3*}, Herman Höfte^{2*}, Kris Vissenberg^{1,10*}
- 8 ¹ Department of Biology, Integrated Molecular Plant Physiology Research (IMPRES), University of
- 9 Antwerp, Antwerp, 2020, Belgium
- 10 Institut Jean-Pierre Bourgin (IJPB), INRAE, AgroParisTech, Université Paris-Saclay, Versailles, 78000,
- 11 France

7

17

20

21 22

24

27

30

- 12 ³ Department of Plant Molecular Biology, The Plant Signaling Mechanisms Laboratory, University of
- 13 Lausanne, Lausanne, 1015, Switzerland
- 14 INRAE, UR1268 BIA, Nantes, 44300, France
- 15 Department of Physics, Politecnico di Milano, Milan, 20133, Italy
- ⁶ Department of Cell Biology and Molecular Genetics, University of Maryland, MD 20742-5815, USA
- Tenter for Mathematics, Computing and Cognition, Federal University of ABC (UFABC), Santo André,
 SP 09606-045, Brazil
 - ⁸ Department of Biosciences, University of Milan, Milano, 20133, Italy
- 23 ⁹ Institute of Biophysics, Consiglio Nazionale delle Ricerche (CNR), Milan, I-20133, Italy
- Department of Agriculture, Plant Biochemistry & Biotechnology Lab, Hellenic Mediterranean University, Heraklion, Crete, PC 71410, Greece
- 28 Lead contact: kris.vissenberg@uantwerpen.be
- 29 Correspondence*: julia.santiago@unil.ch, hermanus.hofte@inrae.fr, kris.vissenberg@uantwerpen.be

Summary

- 31 Pressurized cells with strong walls make up the hydrostatic skeleton of plants. Assembly and
- 32 expansion of such stressed walls depend on a family of secreted RAPID ALKALINIZATION FACTOR
- 33 (RALF) peptides which, curiously, bind both a membrane receptor complex and wall-localized
- 34 LEUCINE-RICH REPEAT EXTENSINS (LRXs) in a mutually exclusive way. Here we show that, in root
- hairs, the RALF22 peptide has a dual structural and signaling role in cell expansion. Together with
- 36 LRX1, it directs the compaction of charged pectin polymers at the root hair tip into periodic
- 37 circumferential rings. Free RALF22 induces the formation of a complex with LORELEI-LIKE-GPI-
- 38 ANCHORED PROTEIN 1 (LLG1) and FERONIA (FER), triggering adaptive cellular responses. These
- 39 findings show how a peptide simultaneously functions as a structural component organizing cell wall
- 40 architecture and as a signaling molecule that regulates this process. This mechanism may also
- 41 underlie wall assembly and expansion in other plant cell types.
 - Keywords: RALF, cell wall, pectin, cell growth, CrRLK1L, LRX, root hair, FERONIA, cell wall integrity

Introduction

The pectic polysaccharides homogalacturonans (HGs), like glycosaminoglycans (GAGs) in the animal extracellular matrix (ECM)¹, are abundant unbranched and charged polymers that play a critical role in the control of the physico-chemical properties of the plant cell wall (CW)². These properties include the remarkable ability to expand while simultaneously resisting the tensile forces imposed by the turgor pressure on the CW².

Pectins are galacturonic acid-containing polymers, which, together with hemicelluloses (e.g. xyloglucans) and (glyco)proteins, form the matrix that surrounds and connects cellulose microfibrils in growing cells³. HGs form the most abundant class of pectins, reaching up to 50% of the total CW polymer content⁴. They are synthesized in a highly methylesterified, uncharged form, and can be demethylesterified by wall-associated pectin methylesterases (PMEs), thus generating random or block-wise anionic charge patterns². *In vivo* studies have associated HG demethylesterification with either the cessation or promotion of cell expansion, depending on the context⁵. Calcium (Ca²⁺)-mediated crosslinking of polyanionic HG has been proposed as a driver for CW stiffening and growth restriction^{6,7}. Growth promotion instead, has been proposed to occur upon the exchange of load-bearing Ca²⁺ crosslinks with newly generated pectate, pectin swelling, or more complex scenarios involving HG turnover or feedback signaling⁸⁻¹⁵. In any case, the physicochemical mechanisms in the pectic CW underlying growth changes remain poorly understood so far.

In this context, it is interesting to note that the properties of the ECM in animals depend not only on the intrinsic physical properties of the GAG polymers but also on the interaction of GAGs and their core proteins with specific GAG binding proteins that modulate their structure¹⁶. For instance, whereas GAGs and GAG-rich proteoglycans promote ECM swelling and generate ultrasoft matrices, the presence of crosslinking proteins leads to water loss, compaction and rigidification of the same matrices¹⁶. In addition, compaction can lead to the transition from a homogenous phase to segregated microphases, as observed for instance for the formation of perineural nets, the porous ECM that wraps neurons¹⁶.

In plants, some *in vitro* evidence shows the interaction of pectin with basic versions of extensins, which are hydroxyproline-rich structural proteins that can form a crosslinked network in the CW. While in *vivo* confirmation is still lacking, these interactions are believed to be partly established by intermolecular di-isodityrosine oxidative crosslinks¹⁷⁻²⁰. Despite the similarities between plant HG and animal GAG polymers, so far it is not known whether pectin-binding proteins contribute to the modulation of CW properties in plants.

Here we show that RALF22, a member of the Rapid Alkalinisation Factor (RALF) family is a driver for the structuration of the CW through its interaction with polyanionic pectin. RALF peptides were first identified by their capacity to induce a rapid alkalinization of the growth medium and are part of a family of 37 members in *Arabidopsis thaliana*^{21,22}. The well-studied peptide RALF23 binds to the GPI-anchored protein LORELEI-LIKE-GPI-ANCHORED PROTEIN 1 (LLG1), thus triggering the formation of a ternary complex with the *Catharanthus roseus* Receptor-Like Kinase1-Like (*Cr*RLK1L) protein FERONIA (FER), involved in immunity signaling²³. RALF4 and 19 are essential for the growth of pollen tubes, in which they activate a module consisting of LORELEI-LIKE-GPI-ANCHORED PROTEIN 2 (LLG2), the *Cr*RLK1L proteins BUDDHAS PAPER SEAL 1 (BUPS1) and ANXUR (ANX1), the cytosolic kinase MARIS and the Ca²⁺ channel of the MILDEW RESISTANCE LOCUS O (MLO) family²⁴⁻²⁷. Related pathways are required for sperm release from pollen tubes, CW integrity control, stress responses or mechanosensing²⁸. Interestingly, several RALF peptides also tightly bind CW proteins of the LEUCINE-RICH REPEAT EXTENSIN (LRX) family, with distinct and mutually exclusive binding modes to the LLG-*Cr*RLK1L signaling system^{27,29-31}. LRXs are dimeric CW proteins, essential for growth, with a RALF-binding LRR domain and a C-terminal extensin domain rich in crosslinkable tyrosines, but without

patches of basic residues that are found in pectin-binding extensins^{29,32}.

- 93 In this study, we used Arabidopsis root hairs (RHs) as a model system to study RALF-mediated pectin 94 structuration and the biological function underlying the existence of two distinct classes of RALF-95 binding proteins. RHs show highly polarized apical growth that can display oscillations in growth rate and a number of other parameters, such as cytosolic Ca²⁺ levels, CW pectin charge, Reactive Oxygen 96 Species (ROS) levels and cytosolic and apoplastic pH³³. This suggests that RH growth is regulated by 97 processes that require, or are optimized by temporal synchronization, eventually leading to the 98 99 emergence of periodicity in CW modifying activities. For instance, processive pectin
- 100 demethylesterification is favored at neutral pH, whereas the remodeling of the cellulose-xyloglucan network by the CW-loosening expansins occurs at low pH^{34,35}. 101
- 102 We show that a periodic CW architecture emerges in RHs from the charge-dependent compaction of 103 polyanionic pectin through its binding to the CW protein complexes LRX1/2-RALF22. In the absence 104 of RALF22 or LRX1/2, the CW architecture is severely perturbed, leading to a frequent loss of cell 105 integrity. Furthermore, when not incorporated into the CW, the same peptide has a signaling role 106 through the formation of a membrane ternary complex with LLG1-FER, which induces cellular
- 107 changes that influence CW assembly and growth.

Results

108

RALF22 is required for root hair growth

- 109 110 To study RALF-regulated cell expansion, we screened publicly available transcriptome data for RH-111 expressed RALF(s). From the seven RALFs that had the highest expression in the primary root (Fig. S1A) only RALF22 transcripts were enriched in RH cells, as shown by single cell RNAseq data (Fig. S1B-112 C), and its expression correlated with the trichoblast developmental stage (Fig. S1D)³⁶. Using CRISPR-113 114 Cas9, we generated a RALF22 loss-of-function line by a 182-nucleotides deletion 51 nucleotides 115 downstream of the start codon (ralf22-1; Fig. 1A). A second loss-of-function allele was identified from 116 the GabiKat seed repository (ralf22-2; GK 293H09; Fig. 1A). Both lines displayed a distinct short and 117 bulged RH phenotype with frequent cell bursting, which was fully complemented by re-introducing 118 the wild-type pRALF22::RALF22 sequence into the mutant genome (Fig. 1B-C; movie 1). 119 Transcriptional reporter lines (Col-0 x pRALF22::GFP) accumulated GFP in RH cells only (Fig. 1D), and 120 showed that RALF22 transcription commenced during RH bulge formation, peaked during tip growth 121 and ceased upon RH maturation (Fig. 1D). These data show that RALF22 is essential for normal RH 122 morphogenesis.
 - RALF22 has FERONIA-dependent and FERONIA-independent effects on root hair

123

124 125 To study RALF22 function, we investigated whether RALF22 is a RH-specific CrRLK1L ligand, similar to other CrRLK1L-binding RALF peptides 24,37,38. Like other RALFs, RALF22 contains a 126 propeptide sequence that is cleaved off by subtilisin-like serine proteases during protein 127 maturation^{39,40}. The mature RALF22 protein harbors two disulfide cysteine-bridges and a 128 conserved YISY motif that is critical for receptor binding (Fig. 2A)^{23,39}. To date, two CrRLK1L 129 receptor-like kinases (ERU, FER) and the FER-RALF23 co-receptor LLG1, were shown to be 130 required for RH morphogenesis 41-43. We recombinantly expressed LLG1 and the ERU and FER 131 132 ectodomains (ERU_{ecd}, FER_{ecd}) in insect cells and purified them for interaction analysis (Fig. S2A-B). 133 In addition, we chemically synthesized RALF22. We then quantified the binding affinities 134 amongst all possible protein combinations (Fig. S2C) using microscale thermophoresis (MST). 135 While RALF22 interacted with LLG1 with a dissociation constant (Kd) of 6.09±1.13µM (Fig. 2B), it did not directly interact with ERU_{ecd} or FER_{ecd} alone (Fig. S2C). Preincubated LLG1-RALF22, 136 137 however, formed a high affinity (118.02±59.01nM) ternary complex with FER_{ecd}, but not with $\mathsf{ERU}_{\mathsf{ecd}} \, (\mathsf{Fig. 2C\text{-}D}, \, \mathsf{Fig. S2C}). \, \, \mathsf{Next}, \, \mathsf{we} \, \, \mathsf{substituted} \, \, \mathsf{both} \, \, \mathsf{tyrosines} \, \, \mathsf{with} \, \, \mathsf{alanines} \, \mathsf{in} \, \, \mathsf{the} \, \, \mathsf{conserved} \, \, \mathsf{$ 138 RALF22 YISY motif (RALF22 Y75A, Y78A) that mediates receptor binding²³. Compared to wild type 139 RALF22, we observed a 4.7-fold decrease in the affinity of RALF22 Y75A,Y78A for LLG1 140

141 (28.48 \pm 2.43 μ M) (Fig. 2B). In addition, LLG1-RALF22^{Y75A,Y78A} no longer formed a ternary complex 142 with FER_{ecd} (Fig. 2C). Together, these results show that RALF22, like RALF23²³, binds to LLG1 and 143 nucleates the formation of a ternary LLG1-RALF22-FER_{ecd} complex.

144

145

146

147

148

149

150

151

152153

154

155

156

157

158159

160

161

162

163

164

165166

167

168

169

170171

172

173

174

175

176

177

178179

180

181

182

183

184

185 186

187

188

Next, we explored the in vivo relevance of this interaction for RH growth. We optimized a protocol that allowed us to reproducibly treat growing RHs while imaging key parameters related to RH elongation, namely oscillations in growth rate, extracellular pH (pH_{ext}) and intracellular calcium ([Ca²⁺]_{cvt}). To this end, we grew Col-0 and FERONIA loss-of-function (fer-4) seedlings expressing the cytosolic Ca²⁺ indicator GCaMP3⁴⁴ in microfluidic chips in the presence of FITC (pH-sensitive) and TRITC (pH-insensitive) coupled to 110kDa and 20kDa neutral dextran, respectively. In animal systems, FITC or TRITC coupled to dextrans of different sizes are commonly used for permeability studies^{45,46}. Here, the large dextran molecules restrict both fluorophores to the extracellular medium and the FITC/TRITC ratio provides a ratiometric quantification of the pHext (Fig. S3A). Using confocal microscopy, we monitored Col-0 and fer-4 RHs before and after administration of 5µM RALF22. During steady-state growth, both Col-0 and fer-4 RHs displayed oscillations in growth rate, [Ca²⁺]_{cvt} and pH_{ext} (Fig. 2E, F). Upon RALF22 treatment, Col-O RHs immediately stopped growing (Fig. 2E, G). This growth arrest was accompanied by a transient spike in [Ca²⁺]_{cvt} (Fig. 2E, H) and an increase in pH_{ext} (Fig. 2E, I), which rapidly spread from tip to shank (Fig. S3B-D). The pH remained high over the next 6 min (Fig. 2E, movie 2). Surprisingly, RALF22 treatment induced a clear migration and accumulation of both dextran-coupled TRITC and FITC fluorophores into the CW, at a comparable rate, suggesting a change in the physicochemical properties of the CW (Fig. 2E, J, movie 2). Upon RALF22 treatment, fer-4 RHs showed a mild growth inhibition and an increase in [Ca²⁺]_{cyt} and pH_{ext} (Fig. 2F-I). In striking contrast to Col-O RHs the extracellular alkalinization did not propagate towards the shank (Fig. S3B, E), while growth rate, [Ca²⁺]_{cyt} and pH_{ext} oscillations recovered rapidly (Fig. 2F-I, movie 2). Crucially, the RALF22-induced migration and accumulation of dextran-coupled TRITC and FITC into the CW was still apparent in fer-4 RHs (Fig. 2F, J; movie 2), suggesting that besides its FER-dependent signaling role, RALF22 treatment has an additional FER-independent effect on the physicochemical properties of the CW.

RALF22 interacts with demethylesterified homogalacturonan and induces its compaction

To understand this FER-independent effect of RALF22 on the CW, it is interesting to note that mature RALF22 is a positively charged protein (isoelectric point = 10.53) (Fig. 3A), which potentially interacts electrostatically with poly-anionic demethylesterified homogalacturonan (HG) in the CW. We used MST to study the interaction between RALF22 and a fully demethylesterified oligogalacturonide, with a degree of polymerization between 7 and 13 (OG7-13) 47 . We observed a robust interaction with a Kd of 3.03 \pm 0.53 μ M (Fig. 3B). The charge dependency of the interaction is suggested by the 3.7-fold reduction in affinity (Kd = 11.1±2.65μM) for a mutant peptide RALF22^{R82A,R90A,R100A} in which 3 charged arginines were replaced by neutral alanine residues (Fig. 3B). To further explore this interaction, we used Quartz Crystal Microbalance with Dissipation monitoring (QCM-D). This technique measures the mass and viscoelasticity of polymer layers deposited on gold-coated oscillating quartz crystals, where a decrease in oscillation frequency (ΔF) linearly correlates with a mass increase and a decrease in the dissipation time of the oscillation after interruption of the current (ΔD) correlates with an increase in viscoelasticity of the layer (Fig. 3C)⁴⁸. In our experimental setup, we first created a pectin layer on the quartz surface (Fig. S4A, B). To this end, the gold-coated quartz, which previously had been spin-coated with a positively charged polymer (poly-allylamine hydrochloride, PAH), was placed in a flow cell and a pectin solution was flown over the surface with a constant flow rate, while monitoring ΔF and ΔD (Fig. S4A, B). As expected, an elastic

191

192

193

194 195

196

197

198

199 200

201

202

203

204

205206

207

208

209

210

211

212213

214

215

216

217218

219

220

221

222

223

224

225

226

227

228

229

230

231

232233

234

235

236

237

pectin layer was formed as shown by the decrease in ΔF_{pectin} and increase in ΔD_{pectin} , both for pectin with a degree of methylesterification (DM) of 75% (DM75, Fig. S4A) and 31% (DM31, Fig. S4B; see Fig. S4C, D for a detailed characterization of the pectin preparations). After a washing step, RALF22 was applied to the DM75 pectin layer (Fig. 3D, Fig. S4A). Unexpectedly, this showed a mass decrease (seen as an increase in ΔF_{RALF22} corresponding to a 9.60±2.22% loss of the mass of the hydrated pectin layer, n=14) and a concomitant increase in stiffness (seen as a decrease in ΔD_{RALF22} corresponding to a 34.05±6.63% decrease in viscoelasticity of the pectin layer, n=14) (Fig. 3D, G). These results indicate that RALF22 interacts with pectin, but also induces water loss from the pectin layer, the mass of which exceeds the gain in mass due the binding of the 5.6 kDa RALF22 peptide. This causes stiffening of the layer, which is expected for the formation of a polyelectrolyte complex where the neutralization of the charges causes dewatering^{49,50}. This interaction was stable under the experimental conditions used since no important changes in ΔF and ΔD were observed during the subsequent washing step (Fig. 3D, Fig. S4A). The charge dependence of the interaction was confirmed by the increased dewatering capacity of RALF22 on pectin with a lower degree of methylesterification (DM31; increase in ΔF_{RALF22} of 38.98 \pm 4.27%, decrease in ΔD_{RALF22} of 94.13 \pm 8.36%, n=15) (Fig. 3E, G, Fig. S4B) as well as the strongly reduced dewatering capacity of mutant peptide RALF22^{R82A,R90A,R100A} (increase in ΔF of $3.53\pm0.24\%$, decrease in ΔD of $13.11\pm1.64\%$, n=2) relative to wild-type RALF22 (Fig. 3F, G). The interaction with fully methylesterified HG could not be assessed using this technique since such polymers do not bind the PAH layer. Together, these results show that, in vitro, RALF22 binds and dewaters pectin in a charge-dependent manner. The formation of such a polyelectrolyte complex not only creates denser zones in the gel, but also augments the porosity of the noncompacted zones^{16,49,50}. An analogous process is thought to underlie the formation of perineural nets, the porous aggregated matrix wrapped around the surface of neurons, which is formed through the interaction between charged GAGs and crosslinking proteins 16. Similar RALF22induced physicochemical changes (pectin charge neutralization, water loss and porosity increase) could account for the FER-independent accumulation of FITC- and TRITC-dextran in the CW of growing RHs (Fig. 2E, F, J; movie 2).

RALF22 forms periodic circumferential rings in the root hair cell wall

To investigate how endogenous RALF22 regulates cell expansion, we generated ralf22-2 lines expressing mCherry-tagged mature RALF22 (ralf22-2 x pRALF22::mCherry-RALF22_{mature}; see Star Methods). Ralf22-2 x pRALF22::mCherry-RALF22_{mature} seedlings had RHs that were indistinguishable from Col-0, showing that the tagged protein is fully functional (Fig. 4A, B). Surprisingly, mCherry-RALF22 accumulated in the RH CW, where it formed regularly spaced microdomains (Fig. 4C), which remained immobile throughout RH development (Fig. 4C, D, movie 3A). These microdomains arise at the RH tip, the exclusive site of RALF22 secretion (Fig. 4E, movie 3B). Indeed, using Fluorescence Recovery After Photobleaching (FRAP) we found that mCherry-RALF22 fluorescence rapidly recovered at the tip, but did not recover subapically (Fig. 4F, movie 4). At the growing apex, de novo mCherry-RALF22 deposition oscillated in antiphase with the growth rate oscillations, illustrating that temporal growth rate periodicity is translated into spatial periodicity in RALF22 microdomain formation in the CW (Fig. 4G). Closer inspection of the mCherry-RALF22 microdomains, using spinning disk microscopy, revealed that they represent regularly spaced rings surrounding the RH's tubular structure (Fig. 4H). These rings first appear at the tip, after which they circumferentially expand 11.5±0.9-fold (n=8) in the expanding dome.

To better understand this localization pattern, we compared the spatial periodicity of mCherry-

RALF22 rings along the RH's longitudinal axis with the temporal periodicity in RH growth rate

(Fig. S5A-D). Based on wavelet transformation of the longitudinal fluorescence pattern present in

the mCherry-RALF22 kymographs (e.g. Fig. 4D) the average RALF22 ring spacing was 1.34±0.08

- 238 μm (Fig. S5A, B). Interestingly, for the same RHs, a single growth rate period (30.47±0.93s at
- 239 2.15±0.06 µm.min⁻¹) attributed to an average RH length gain which was 1.21-fold lower
- 240 (1.09 \pm 0.04 μ m.period⁻¹; Fig. S4C-E), suggesting that the spacing between RALF22 rings increases
- when moving from tip to shank. We then used wavelet analysis to compare the mCherry-RALF22
- 242 ring spacing in the expanding dome and along the RH shank (Fig. 4I, Fig. S5F-K). Indeed, whilst
- 243 the spacing in the tip was 0.94±0.08 μm, shank-localized rings were spaced 1.37-fold further
- 244 apart at 1.29±0.08 μm (Fig. 4I, Fig. S5J, K).
- 245 Together, these data show that, during RH growth, the temporal periodicity in growth rate
- 246 translates into the spatial periodicity in RALF22 ring formation in the CW. In addition, wall
- 247 expansion over the surface of the dome was highly anisotropic as shown by the 8.4x larger
- 248 circumferential strain (11.5-fold increase) of the rings relative to the meridional (from tip to
- shank) strain (1.37-fold increase).

RALF22 forms a complex with LRX1 in root hair cell walls

251 The periodic arrangement of RALF22 in the RH CW suggests that it could associate with other

- 252 CW epitopes with a similar ring-like organization. Interestingly, RALF-mediated regulation of CW
- integrity depends on two distinct receptor families, the biological relevance of which is unclear.
- 254 Hence, RALF peptides have previously been shown to bind CW proteins of the LEUCINE-RICH
- 255 REPEAT EXTENSIN (LRX) family, with distinct and mutually exclusive binding modes to the LLG-
- 256 CrRLK1L signaling system^{23,27,29-31}. In RHs, LRX1 and LRX2 have partially redundant roles in
- sustaining RH growth⁵¹. The RH phenotype of the *lrx1-1/2-1* loss-of-function mutant is
- 258 indistinguishable from ralf22, suggesting that they could be functionally related (Fig. 5A, B,
- 259 movie 5). To investigate the plausibility of a RALF22-LRX1/2 complex, we generated a peptide
- docking model using the crystal structure of the LRR domain of LRX2 (LRX2_{LRR}, PDB: 6QXP)²⁹ and
- an AlphaFold2 model of the corresponding LRX1_{LRR} domain (Fig. 5C). RALF22_{mature} was modelled
- using the crystal structure of RALF4 (PDB: 6TME) as a reference. Similar to the LRX8_{LRR}-RALF4
- 263 complex²⁹, we found that the conserved binding pockets of LRX2_{LRR} and LRX1_{LRR} could
- accommodate RALF22_{mature} (Fig. 5C, LRX2_{LRR}-RALF22; total energy score=-66.43 kcal.mol⁻¹; root
- mean square deviation=0.760 Å). LRX1_{LRR}-RALF22 and LRX2_{LRR}-RALF22 dimeric complexes could
- indeed be purified from insect cells that co-expressed LRX1_{LRR} or LRX2_{LRR} with RALF22 (Fig. 5D).
- 267 These complexes were extremely stable as shown by the inability of LRX1_{LRR}-RALF22 to dissociate
- 268 at pH 2.0 (Fig. 5D, E) and their 92.3°C (LRX1_{LRR}-RALF22) and 83.8°C (LRX2_{LRR}-RALF22) dissociation
- temperatures in thermal shift assays (Fig. 5F). These results suggest that the LRX1_{LRR}-RALF22 and
- 270 LRX2_{LRR}-RALF22 are bona fide complexes with even higher stability than the previously described
- 271 LRX8_{LRR}-RALF4 pollen expressed complex²⁹.
- 272 To study the LRX1-RALF22 interaction in planta, we introduced pRALF22::mCHERRY-RALF22_{mature}
- 273 into Irx1-1 plants that express a functional cMyc-tagged LRX1 (Irx1-1 x pLRX1::cMyc-LRX1⁵²).
- 274 cMyc-LRX1 also formed rings perpendicular to the RH's longitudinal axis, that colocalized to a
- great extent with mCHERRY-RALF22_{mature} (Fig. 5G, H; Costes p-value>0.95; thresholded Manders'
- coefficient (tM)_{mCHERRY-RALF22@cMvc-LRX1}=0.71±0.22; tM_{cMvc-LRX1@mCHERRY-RALF22}=0.70±0.21; n=11). These
- data are consistent with the presence of LRX1-RALF22 complexes *in planta* but are expected to
- be incomplete given the presence of endogenous RALF22 and LRX2. Together, these data show
- 279 that RALF22 adopts a periodic pattern in the RH CW at least in part as an LRX1-RALF22 complex.

280 LRX1-RALF22 also binds and compacts demethylesterified homogalacturonan

- 281 Next, we investigated whether pectin binding is preserved in the LRX1_{LRR}-RALF22 complex. A
- possible pectin interaction is suggested by the 3D crystal structure of the LRX8_{IRR}-RALF4 dimer, in
- which RALF4 displays a highly positively-charged and surface-exposed patch of amino acids²⁹.
- Homology modeling shows that this is also true for the LRX1_{LRR}-RALF22 complex, albeit with a
- 285 less pronounced surface charge compared to LRX8_{LRR}-RALF4 (Fig. 5C), comprising the three

arginines (R82, R90, R100) that are critical for free RALF22-pectin binding (Fig. 3B, F, G, Fig. 5C). QCM-D indeed showed an interaction of the LRX1_{LRR}-RALF22 complex with DM75 and DM31 pectin layers (Fig. 5I-K). In contrast to free RALF22 however, we observed a charge-dependent mass increase (decrease in $\Delta F_{LRX1-RALF22}$ for DM31 of 278.21±26.64%, n=11; decrease in $\Delta F_{LRX1-RALF22}$ RALF22 for DM75 of 98.62±31.52%, n=6) (Fig. 51-K). Together with the mass increase, we observed a decrease of the viscoelasticity ($\Delta D_{LRX1-RALF22}$ decrease for DM31 of 48.02±15.06%, n=11; $\Delta D_{LRX1-RALF22}$ RALF22 decrease for DM75 of 22.54±7.37%, n=6), indicating that LRX1LRR-RALF22, like free RALF22, promoted the stiffening of the pectin layers (Fig. 5K). Concerning the LRX1_{LRR}-RALF22-dependent mass increase, as opposed to the mass decrease observed upon free RALF22 supply, this is most likely due to the much higher mass of the LRX1_{LRR}-RALF22 dimer (94.18kDa) compared to the mass of RALF22 alone (5.6kDa), which most likely exceeds the mass loss due to pectin dewatering. The observed decrease in ΔD is presumably the resultant of the stiffening effect of the LRX1_{LRR}-RALF22-pectin interaction and the decrease in viscoelasticity due to the addition of extra mass to the layer. More detailed studies are needed to quantify these different effects. Nevertheless, these results show that LRX1_{LRR}-RALF22, like free RALF22, is able to bind and stiffen pectin in a charge-dependent manner.

RALF22 is required for the self-assembly of pectic homogalacturonan

Given the charge-dependence of the interaction of RALF22 and LRX1-RALF22 with pectin, pectin demethylesterification is expected to be critical for the assembly and expansion of the RH CW. To investigate this, we first supplemented growing RHs with the PME inhibitor EGCG, while imaging [Ca²+]_{cyt}, pH_{ext} and CW charge (Fig. S6; movie 6). EGCG treatment induced a short decrease in growth rate, followed by a transient growth spurt and a transition from longitudinal to radial expansion (=swelling) at the tip (Fig. S6A; movie 6). This response was accompanied by a transient increase in propidium iodide staining, a dye that stains charged polymers in the CW⁵³, and high amplitude [Ca²+]_{cyt} and pH_{ext} transients that coincided with rapid tip swelling (Fig. S6A; movie 6). No such changes were observed upon mock treatment (Fig. S6B, movie 6). Together these observations underscore the dynamic nature of pectin metabolism in growing RHs, where rapid feed-back signaling compensates the effect of the inhibition of PME activity, at least in part through the alkalinization of the cell surface. The latter is expected to promote PME activity, given the high pH optimum of plant PMEs³4. The radial expansion of the RH tip as rapid as one minute after EGCG treatment emphasizes the critical role for pectin demethylesterification in maintaining polar growth of RHs.

Next, we hypothesized that preventing pectin demethylesterification in the RH CW would also affect the cell's response to RALF22 treatment. To test this, we measured $[Ca^{2+}]_{cyt}$ responses upon RALF22 treatment, in the presence or absence of EGCG, in seedlings expressing the G5A BRET sensor driven by the RH-specific promoter pEXPa7⁵⁴. This assay, in contrast to the observation of individual RHs in microfluidic chips (Figure 2; movie 2), is more suitable for gathering quantitative data from large numbers of treatments. We found that a treatment as short as 30 min, at an EGCG concentration close to the EC₅₀ for root growth inhibition (32 μ M⁵⁵), greatly reduced the subsequent RALF22-induced [Ca²⁺]_{cyt} transient (Fig. S6C, D), showing that, also *in vivo*, pectin demethylesterification is crucial for RALF22 function.

To further investigate the *in vivo* connection between the methylesterification status of HG and the periodic organization of (LRX1-)RALF22 in the CW, we labeled *ralf22-2* x *pRALF22::mCherry-RALF22_{mature}* RHs with monoclonal antibodies (mABs) directed against different HG epitopes (Fig. 6, Fig. S7). LM20, which labels methylesterified HG⁵⁶, was enriched at the tip and labeled sparse patches along the RH shank (Fig. S7A-C), corroborating that methylesterified HG is deposited and demethylesterified in the expanding dome. Interestingly, LM20 labeled an outer layer of the CW that was devoid of mCHERRY-RALF22_{mature}, which localized closer to the plasma membrane both

in the tip and the shank (Fig. S7A, B). The mAb 2F4, an IgG1 that binds to Ca2+-crosslinked demethylesterified HG⁵⁷, labeled the RH tip and shank and, like LM20, preferentially labeled an outer layer of the CW, which only partially overlapped with mCherry-RALF22_{mature} (Fig. S7D, E; Costes p-value>0.95; $tM_{mCHERRY-RALF22@2f4}=0.56\pm0.04$; $tM_{2F4@mCHERRY-RALF22}=0.49\pm0.02$; n=8). Also along the shank, Ca²⁺-crosslinked demethylesterified HG was organized in rings, where regions with a relatively lower mCherry-RALF22_{mature} abundance appeared to show higher 2F4 labeling and vice versa (Fig. S7E, F). Finally, PAM1, a small HIS-tagged scFv mAb directed towards long (>30DP) stretches of block-wise demethylesterified HG⁵⁸, labeled the RH CW both in the tip and shank (Fig. 6A-D). In contrast to LM20 and 2F4 epitopes, this epitope revealed circumferential rings in the RH CW that largely overlapped with mCherry-RALF22_{mature} (Fig. 6A-D; Costes pvalue>0.95; $tM_{mCherry-RALF22 \rightarrow PAM1}$ =0.74±0.05; $tM_{PAM1 \rightarrow mCherry-RALF22}$ =0.74±0.04; n=12). These results, in accordance with the charge-dependence of the (LRX1-)RALF22-pectin interaction (Fig. 3B, D-G, Fig. 5I-K, Fig. S6C, D), show that newly secreted pectin, upon demethylesterification, interacts with (LRX1-)RALF22 in muro where it becomes part of periodic rings (Fig. 6A-D). The periodic CW pattern could indicate that mCherry-RALF22_{mature} associates with a preexisting HG pattern in the CW or that the (LRX1-)RALF22 interaction with demethylesterified HG could be

The periodic CW pattern could indicate that mCherry-RALF22_{mature} associates with a preexisting HG pattern in the CW or that the (LRX1-)RALF22 interaction with demethylesterified HG could be responsible for inducing the formation of periodic pectin rings. To investigate this possibility, we labeled the CW of *ralf22-2* RHs with anti-HG antibodies (Fig. 6E, F). Interestingly, in *ralf22-2*, the abundance of block-wise demethylesterified HG (PAM1) and Ca²⁺-crosslinked demethylesterified HG (2F4) was reduced by 68±3% and 46±7% respectively, relative to Col-0 (Fig. 6E, F). In addition, methylesterified HG (LM20), showed a 95±3% and 85±16% reduced labeling in the *ralf22-2* tip and shank, respectively, as compared to Col-0 (Fig. 6E, F). Combined, these data illustrate that, in the absence of RALF22, overall pectin secretion is reduced and/or turnover is enhanced.

We then investigated the requirement of LRX1/2 for the periodic organization of the pectic CW by studying the RHs of the double Irx1-1/2-1 mutant expressing mCherry-RALF22_{mature} (Irx1-1/2-1 x pRALF22::mCherry-RALF22_{mature}, Fig. 6G-I, movie 7). These RHs, like those of the untransformed Irx1-1/2-1 parent, grew slowly and frequently burst. In surviving Irx1-1/2-1 RHs, most mCherry-RALF22_{mature} accumulated in intracellular compartments, yet a small amount was still secreted to the CW (Fig. 6G, movie 7). CW labeling was 3.5- and 2.5-fold weaker in the tip and shank CW respectively, compared to the complemented ralf22-2 x pRALF22::mCherry-RALF22_{mature} line (Fig. 6G, H, movie 7). Interestingly, in the absence of LRX1 and LRX2, mCherry-RALF22_{mature} and PAM1 organization showed a much more fragmented pattern compared to the control (Fig. 6D, I). Moreover, in the Irx1-1/2-1 CW, demethylesterified HG accumulated 2.4-fold, relative to the WT, at the tip, but not in the shank (Fig. 6G, H). Given that pectin secretion occurs at the tip, this suggests an increased pectin secretion and turnover in the absence of LRX1/2. Moreover, the PAM1 epitope and mCherry-RALF22_{mature} showed only limited colocalization in the shank of Irx1-1/2-1 RHs (Fig. 6I; Costes p-value>0.95 for 4 out of 6 samples; $tM_{mCherry-RALF22_PAM1}=0.25\pm0.08$; tM_{PAM1} smcherry-RAIF22=0.19±0.07; n=6). Together, these results show that the LRX1/2-RALF22 complex, through its binding and compaction of demethylesterified pectin, organizes the patterning of the pectic RH CW. In the absence of this patterning, pectin secretion and turnover are increased and the CW's integrity is compromised.

Discussion

335

336

337

338

339 340

341

342

343

344 345

346

347

348

349

350

351

352

353

354 355

356

357

358

359

360

361

362

363

364

365

366

367

368

369

370

371372

373

374

375

376

377

378 379

380

381

Here, we identified RALF22 as the main trichoblast-expressed RALF peptide controlling growth and CW integrity of RHs. RALF22 binds LRX1 and LRX2, forming extremely stable complexes (dissociation t° > 80°C) *in vitro* (Fig. 5D-F) and, given the colocalization pattern (Fig. 5G-H), most likely also *in vivo*. RALF22 also binds LLG1 and recruits FER into an active membrane-bound ternary signaling complex (Fig. 2B, C). The *in vivo* relevance of this interaction in RHs is shown by

the requirement of FER to induce sustained surface alkalinization and growth arrest upon RALF22 treatment (Fig. 2E-J, movie 2).

384

385 386

387 388

389 390

391

392

393

394

395

396

397 398

399

400

401

402

403

404

405 406

407 408

409

410

411

412413

414

415

416

417

418

419

420

What is the functional relevance of the existence of two distinct, mutually exclusive binding partners²⁹ for the same peptide at the surface of the same cell? This report provides an answer to this key question by showing that RALF22 is not only a signaling peptide, but that it also has a structural role (Fig. 7). Indeed RALF22, as a free peptide or bound to LRX1, binds demethylesterified pectin *in vitro* (Fig. 3B-G, Fig. 5I-K). Pectin binding is also relevant *in vivo*, as suggested by (i) the diminished [Ca²⁺]_{cyt} response upon RALF22 treatment of RHs pretreated with EGCG (Fig. S6C, D), (ii) the colocalization of mCHERRY-RALF22 with blockwise demethylesterified HG (PAM1 epitope; Fig. 6A-D), but not with highly methylesterified HG (LM20 epitope; Fig. S7A-C), in the RH CW, where it forms stable microdomains organized in periodic concentric rings (Fig. 4C-I, Fig. S5) and (iii) the loss of proper pectin organization in the absence of RALF22 or LRX1/2 (Fig. 6E-I).

A mechanism for microdomain formation is suggested by the capacity of free RALF22 and LRX1_{LRR}-RALF22 to induce the compaction of a pectin layer. The charge-dependence of this interaction suggests that the free unstructured and positively-charged peptide induces water loss through the neutralization of the pectin charges and the resulting loss of osmotically active counterions in the pectin gel. The interaction of the LRX1_{LRR}-RALF22 hetero-tetramer with pectin may be more complex, since here the peptide is folded and exposes a structured surface with positively charged residues that, besides electrostatic interactions, may also recognize structural features of the polysaccharide, such as charge patterns, as reported for instance for GAG-binding proteins in the animal ECM^{1,59}, or acetyl⁶⁰ or xylosyl⁶¹ substitution motifs. In addition, the LRX1_{LRR}-RALF22 dimer may promote polymer crosslinking, thus reducing the water binding capacity (Fig. 3D-G, Fig. 5I-K, Fig. S4A, B)⁶². Compaction of GAGs by GAG cross-linking proteins creates denser zones in the gel, but also augments the porosity of the non-compacted zones as observed during the formation of perineural nets, the porous aggregated matrices surrounding neurons¹⁶. A similar process may explain why RALF22 supplementation triggers the migration of dextran-coupled FITC and TRITC to the RH CW (Fig. 2E, F, J, movie 2). It should be noted that, besides the RALF22-binding LRR domain, LRX1 also comprises a C-terminal extensin domain. At least one extensin family member, AtEXT3, was able to polymerize into a scaffold in vitro thanks to its amphiphilic properties⁶³. The authors hypothesized that this scaffold could form coacervates with pectin, due to its repeated basic domains, and thus structure the CW. This polymer network could then be consolidated by intermolecular oxidative crosslinking of the extensin's tyrosine residues. Interestingly, since the extensin domain of LRX1 itself does not have such basic domains, RALF22 may play this pectin-recruiting role in the complex. The advantage of such a modularity might be twofold: first the same LRX could bind different CW polysaccharides or polysaccharide motifs by switching RALF isoforms, perhaps promoting different CW architectures, and second, free RALF peptide may be part of a FER-dependent feedback signaling mechanism that coordinates its own incorporation into the CW.

421 This study provided striking new insights into the logic of RALF feedback signaling. Whereas 422 RALF22 treatment resulted in a dramatic change in the physicochemical properties of the CW, 423 the cell required FER to induce a normal pH and growth response (Fig. 2E-J, Fig. S3B-E, movie 2). 424 One way to explain these results is by assuming that the LLG1-RALF22-FER complex acts as a 425 mechano-sensor, which responds to CW compaction induced by (LRX1-)RALF22. In other words, 426 (LRX1-)RALF22 at the same time creates a signal (CW compaction) and controls the sensitivity of 427 the detection system, possibly through LLG1-RALF22-FER recruitment. A role for LLG1/FER in mechano-sensing has been proposed previously 64-66. For instance, stretched epidermal cells 428

upon root bending displayed biphasic cytosolic Ca²⁺ responses, with a rapid transient and a slower more sustained component. Only the latter disappeared in *llg1* and *fer* mutants⁶⁵, whereas the initial transient might come from another mechanosensor, such as a mechanosensitive Ca²⁺-permeable channel⁶⁷. Similarly in RHs, we observed that in *fer-4*, RALF22 still induced a transient growth inhibition and surface pH increase at the tip, after which growth, pH and [Ca²⁺]_{cyt} oscillations resumed, in contrast to the wild type, where the surface alkalinisation propagated along the shank and growth did not recover (Fig. 2E-J, Fig. S3B-E, movie 2). Mechanosensing in the leaf epidermis also appears to depend on FER, where it signals through the activation of ROP6 by FER-bound ROPGEF14⁶⁵. This in turn is thought to affect microtubule and actin dynamics and secretion. Interestingly, we observed an over 90% reduction in methylesterified (LM20) pectin at the RH tip of *ralf22* and an over two-fold increase of the epitope in *lrx1/2* (Fig. 6H, I). This suggests that free RALF22, which is absent in *ralf22* and expected to be more abundant in the absence of LRX1/2, may promote the secretion of pectin at the tip.

RALF22-induced and FER-dependent sustained alkalinization is also expected to promote HG demethylesterification given the alkaline pH optimum of PMEs³⁴. Together, free RALF22 might signal the need for more polyanionic pectin as a substrate for the CW-structuring LRX1-RALF22pectin complexes. In this context it is of interest to note that the spacing of the CW microdomains in the RH tip matched the length increase during a growth/surface pH oscillation cycle (Fig. 41, Fig. S5), and that apical RALF22 deposition oscillated in antiphase with the growth rate (Fig. 4G). This supports the idea that CW assembly is a cyclic process in RHs along the following scenario (Fig. 7): first, wall material, including methylesterified HG and LRX1-bound and free RALF22, is deposited at the tip of the growing RH. A concomitant or subsequent increase in CW pH through the binding of free RALF22 to LLG1/FER, activates processive pectin methylesterase (PME) activity, thus exposing stretches of negative charges on the polymer. This creates the substrate for the interaction with the LRX1/2-RALF22 dimer causing the dewatering of the pectin gel and the formation of a ring-like structure of higher density surrounding the RH tip. This structure is organized in such a way that it favors CW expansion in the circumferential direction. This deposition-demethylesterification-compaction-expansion process is repeated during each growth cycle. Given that cellulose⁶⁸, xyloglucan⁶⁹ and expansins⁷⁰ are essential for RH growth, it will be interesting to see if expansin-mediated acid growth contributes to the preferentially circumferential expansion of the ring and whether this involves purely remodeling of the existing structure or the insertion of additional material. Further studies using microscopy at high spatio-temporal resolution¹¹, should provide more insights into this fascinating CW assembly process in RHs and most likely in other cell types in plants.

Acknowledgments

This work was funded by the Research Foundation Flanders (FWO; grants 1225120N and G013023N), the University of Antwerp (UA; BOF-KP; DOCPRO4) and LASERLAB-EUROPE (grant 654148) to SS and KV; the Agence Nationale pour la Recherche (ANR), project "HOMEOWALL" to HH; and the University of Lausanne, the European Research Council (ERC) grant agreement no. 716358 and the Swiss National Science Foundation grant 310030_204526 to JS. The authors would like to thank Jozef Mravec for sharing OG7-13, and Christoph Ringli, Alice Cheung and Simon Gilroy for kindly donating Irx1-1/2-1 and Irx1-1 x pLRX1::cmyc-LRX1, fer-4 x pFER::FER-GFP, and Col-0 x 35S::GCaMP3 seeds, respectively. Tou Cheu Xiong in thanked for providing the G5A Ca²⁺ sensor line. Our gratitude also goes to CPKelco (Denmark) for donating industrial low and high methoxyl pectin samples. The IJPB benefits from the support of Saclay Plant Sciences-SPS (ANR-17-EUR-0007). This work has benefited from the support of IJPB's Plant Observatory technological platforms. Access to fluorescence

- 476 microscopy infrastructure was provided by the Antwerp Centre for Advanced Microscopy (ACAM,
- 477 UA). The purchase of the PerkinElmer UltraVIEW Vox and Leica SP8 confocal microscopes was
- 478 supported by FWO-HERCULES infrastructure grants; AUHA-09-001, AUHA-15-12. The Nikon Sora
- 479 microscope was purchased with the support of an FWO mid-size infrastructure (I003420N) and FWO
- 480 IRI grant (I000123N).

497

499 500

501

502

503

504

505

506

507

508

509

510

511512

513

514

515516

517

518

519

520

521

Author contributions

- 482 S.S., K.V., H.H. and J.S. conceived the project. S.M. aided in conceptualizing the research based on his
- 483 work on LRX8-RALF4. J.K.L. and J.S. designed, produced and characterized all recombinant proteins.
- 484 C.B. provided technical assistance for protein production. E.F. and M.G. designed and performed
- 485 calcium assays using the G5A BRET sensor. S.S. generated all crosses and performed the cloning of
- 486 the pEXPa7::G5A sensor and RALF22-related constructs. S.S. optimized microfluidics for imaging and
- performed the phenotyping, staining and imaging of live cell and fixed-tissue samples. S.S. performed
- image analysis, bio-informatics and statistics. N.C. assisted with live cell imaging, cloning and sample
- preparations. D.B. assisted with cloning, phenotyping and sample preparation. S.S. and M.G.
- 490 performed Microscale Thermophoresis analysis. H.H. and B.C. conceived the QCM-D analysis. T.L. and
- 491 H.H. performed the QCM-D analysis. T.L. characterized the pectin solutions. E.B. and C.M. provided
- 492 technical and conceptual assistance with the *in vitro* QCM-D and pectin work. H.A. aided in
- conceptualizing the work and provided assistance with sample preparation for phenotyping. A.B.,
- 494 A.C., D.S.C.D and J.F. aided in the visualization and analysis of oscillatory parameters in live cell
- imaging. J.S. generated 3D protein structures and performed peptide docking modelling. S.S., H.H.
- 496 and K.V. wrote the manuscript.

Declaration of interests

The authors declare no competing interests.

Figure legends

Figure 1. RALF22 regulates root hair growth. (A) scheme of the *RALF22* genomic sequence showing the T-DNA insertion site of GabiKat line GK_293H03 (*ralf22-2*) and the 182 nucleotide-long deletion in *ralf22-1*. (B) representative 6-day-old roots of Col-0, *ralf22-1* (-/-), *ralf22-2* (-/-) and *ralf22-2 x pRALF22*::*RALF22* (COMP) seedlings (scale bar=500µm). Close-ups of RHs showing the short, bulged and burst (cfr. movie 1) *RALF22* loss-of-function phenotype (scale bar=100µm). (C) graph showing the mean RH length (±SEM) and % of RH bursting for all genotypes (n≥5, ***p<0.001). Three independent complementation lines (*ralf22-2 x pRALF22:RALF22*) are shown. (D) representative confocal maximal projections and transverse optical sections of 6-day-old Col-0 seedlings expressing GFP under the control of the *RALF22* promoter (Col-0 x *pRALF22::GFP*). *RALF22* is transcribed in trichoblast cells throughout RH growth (scale bars= left, 100µm; middle, 50µm; right; 25µm).

Figure 2. RALF22 binds to FERONIA to regulate root hair growth. (A) model of mature RALF22 showing the conserved YISY domain (sticks) required for LLG binding. (B) MST results showing the binding affinity between fluorescently labelled recombinant LLG1 and RALF22 (n=7) or RALF22 Y75A,Y78A (n=3). (C) Binding affinity between the FERONIA ectodomain (FER $_{ecd}$) and fluorescently labelled LLG1 preincubated with RALF22 (n=3) or RALF22 Y75A,Y78A (n=3). MST values are represented as the average normalized change in fluorescence (%) \pm SEM. (D) Homology model of the LLG2-RALF22-FER $_{ecd}$ complex. The N-terminal region of RALF22 was docked into the LLG2 structure (PDB:6A5E). FER $_{ecd}$ was superimposed based on the crystal structure. The YISY motif is highlighted in sticks. (E-F) Timelapse imaging of Col-0 (E) and *fer-4* (F) RHs being treated with 5 μ M RALF22 (cfr. Movie 2). The kymographs and corresponding plots depict changes in the growth rate, [Ca $^{2+}$]_{cyt} (cytosolic GCaMP3 fluorescence intensity), pH_{ext} (extracellular FITC-110kDa dextran/TRITC-20kDa dextran fluorescence intensity ratio)

and migration of fluorescent FITC-110kDa dextran and TRITC-20kDa dextran into the CW (a proxy for altered CW physico-chemistry) during 4min of steady state growth followed by treatment with RALF22. The RH's response to RALF22 was monitored for 6min. Kymographs were generated along the horizontal lines depicted in the insets. (G-J) quantification of the average growth rate (G), $[Ca^{2+}]_{cyt}$ (H), pH_{ext} (I), and FITC or TRITC fluorescence in the CW (J) before, upon and after treatment with RALF22 in Col-0 (n=9) and *fer-4* (n=8) RHs. Col-0 RHs were also treated with a mock solution (-RALF22, n=7). Barplots represent the mean \pm SEM. Different letters represent statistical significance (α =0.05).

Figure 3. RALF22 binds and compacts demethylesterified homogalacturonan. (A) mature RALF22 is a positively charged protein. In bold: the amino acids which are positively charged at pH 7.0. (B) MST affinity plots showing that RALF22 interacts with OG7-13, a 7-13mer long fully demethylesterified oligogalacturonide (n=3). Mutating three cationic arginines on the RALF22 (RALF22^{R82A,R90A, R100A}) surface leads to a 3.7-fold reduction in affinity (n=3). (C) illustration of the QCM-D working principle. An alternating current is applied to a quartz surface which holds the pectin gel. The frequency of the lateral quartz oscillation (*F*) is inversely correlated with the mass of the pectin layer. The time it takes for the lateral oscillation to dissipate (*D*) when the current is interrupted positively correlates with the rigidity of pectin layer. (D-F) Representative ΔF and ΔD QCM-D traces for a pectin layer with a degree of methylesterification of 75% (D) or 31% (E) treated with $1\mu g.mL^{-1}$ RALF22 or DM31 pectin treated with $1\mu g.mL^{-1}$ RALF22^{R82A,R90A, R100A}. Grey zones highlight the intervals during which pectin or RALF were applied (cfr. Fig. S4A,B). (G) Quantification of the % change in ΔF and ΔD upon RALF treatment for the conditions presented in D-F (DM75 + RALF22, n=14; DM31 + RALF22, n=14; DM31 + RALF22^{R82A,R90A, R100A}, n=2). Data is shown as the mean \pm SEM. Different letters represent statistical significance (α =0.05).

Figure 4. RALF22 forms circumferential rings in the root hair cell wall which illustrate anisotropic wall expansion. (A) representative images of 6-day-old Col-0, ralf22-2 and ralf22-2 x pRALF22::mCHERRY-RALF22_{mature} roots (scale bar=500μm) and RHs (scale bar=100μm). (B) quantification of the average RH length and percentage of RH bursting for each genotype (n≥5, ***p<0.001). (C) Representative longitudinal optical section of a growing (left) and a mature (right) ralf22-2 x pRALF22::mCHERRY-RALF22_{mature} RH (scale bar=8µm). ROIs showing the presence of mCHERRY-RALF22_{mature} microdomains in the RH CW (scale bar=2μm). (D) maximal projection kymograph corresponding to a 10min timelapse acquisition of a growing ralf22-2 x pRALF22::mCHERRY-RALF22_{mature} RH. Vertical red lines represent mCHERRY-RALF22_{mature} microdomains that remained stationary in the CW throughout the acquisition. The longitudinal fluorescence pattern for quantification of the mCHERRY-RALF22_{mature} microdomain spacing was extracted along the yellow dotted line. (E) maximal projection kymograph of the RH tip CW after removal of the dome's concave shape. Red lines represent stationary mCHERRY-RALF22_{mature} microdomains, which arise at the very apex and move towards the shank as the tip grows forward. (F) Representative snapshots of a growing ralf22-2 x pRALF22::mCHERRY-RALF22_{mature} RH before, upon and after photobleaching of mCHERRY-RALF22_{mature} in ROIs in the CW of the expanding dome, below the tip and in the shank (scale bar=5µm). Graphs showing mCHERRY fluorescence recovery at the apex only. (G) representative timeseries showing that RH growth rate and apical mCHERRY-RALF22_{mature} fluorescence oscillate in antiphase. (H) frontal and lateral highresolution z-projections of mCHERRY-RALF22_{mature} organization in the RH CW, illustrating the formation of regularly spaced mCHERRY-RALF22_{mature} rings (scale bar=2μm). (I) Representative high resolution longitudinal optical section of a representative growing RH (scale bar=5µm) showing mCHERRY-RALF22_{mature} microdomains in the tip and the shank (scale bar=4μm). Comparative analysis of mCHERRY-RALF22_{mature} microdomain spacing in the tip (n=12) vs. the shank (n=15). Data is presented as the mean ± SEM. Asterisks depict statistical significance (**p<0.01).

Figure 5. RALF22 binds to LRX1 in the root hair cell wall and compacts demethylesterified homogalacturonan. (A) The *lrx1-1/2-1* and *ralf22-2* phenotypes are indistinguishable. Representative

575

576

577578

579

580

581

582

583

584

585

586

587

588

589

590

591

592

593

594

595

596

597

598 599

600

601

602

603

604

605

606

607

608

609

610 611

612

613 614

615

616

617

618

619

620

621

622

623

624

625

pictures (scale bar=500um) and close-ups (scale bar=100um) of 6-day-old seedlings are shown. (B) quantification of the RH length and % of RH bursting of Col-0, ralf22-2 and lrx1-1/2-1 seedlings (n≥5, ***p<0.001). (C) Structural superimposition of the LRX2 (PDB:6QXP; grey) and LRX1 AlphaFold2 model (orange) (top left). Root Mean Square Deviation (R.M.S.D) of 0.15Å comparing 342 pairs of corresponding Cα atoms between the two proteins. Full molecular docking model of RALF22 (green) with LRX2_{LRR} (PDB: 6QXP; grey) (top right). Enlarged view of the peptide docking models showing RALF22 (green) in the LRX2_{LRR} and LRX1_{LRR} (AlphaFold2 model) binding pockets (bottom). The three exposed Arginines (R82, R90, R100) required for pectin binding are depicted as sticks. (D) Size exclusion chromatography of LRX1_{LRR}-RALF22 (pH 5.0 and 2.0) and LRX2_{LRR}-RALF22 (pH 5.0) purified from insect cells, showing that the complex does not dissociate at pH 2. (E) SDS protein gels of the fractions corresponding to the SEC elution peaks for LRX1_{LRR}-RALF22 (pH 5.0 and 2.0) and LRX2_{LRR}-RALF22 (pH 5.0). (F) thermoshift assay of LRX8_{LRR}-RALF4 (control), LRX1_{LRR}-RALF22 and LRX2_{LRR}-RALF22. LRX1_{LRR}-RALF22 was subjected to pH 5.0 and pH 2.0. Low pH does not affect the thermostability of the complex. (G) representative longitudinal optical sections of the lrx1-1 x pLRX1::cMyc-LRX1 x pRALF22::mCHERRY-RALF22_{mature} CW in which LRX1 was labeled with a green fluorescent anti-cMyc antibody (scale bar=5µm). Dots represent cMyc-LRX1 (green) and mCHERRY-RALF22_{mature} microdomains (red). Composite images and magnifications (scale bar=1µm) show colocalization (yellow) between LRX1 and RALF22. (H) Representative lateral z-projections of cMyc-LRX1 (green) and mCHERRY-RALF22_{mature} (red) organization and colocalization (yellow) in the RH CW (scale bar= 5μ m). cMyc-LRX1 colocalizes with RALF22_{mature} rings in the CW. (I,J) representative ΔF and ΔD traces of DM75 (I) and DM31 (J) treated with 10 μg.mL⁻¹ of LRX1_{LRR}-RALF22. (K) Quantification of the % change in ΔF and ΔD (relative to the pectin-induced change) upon LRX1_{LRR}-RALF22 treatment for the conditions presented in I and J (DM31 + LRX1_{LRR}-RALF22, n=11; DM75 + LRX1_{LRR}-RALF22, n=6). Data is shown as the mean ± SEM. Asterisks represent statistical significance (p-value; ***<0.001).

Figure 6. (LRX1-)RALF22-homogalacturonan interaction regulates the organization of the pectic root hair cell wall. (A-D) representative images showing the colocalization of PAM1 (>30DP long stretches of block-wise demethylesterified homogalacturonan) and mCHERRY-RALF22_{mature} in the RH tip and shank. (A) longitudinal optical sections of a PAM1 (green) and mCHERRY-RALF22_{mature} labeled RH (scale bar=10µm), which was fixed while growing. Yellow indicates colocalization in the composite image. (B) close-ups of RH tip presented in A showing that PAM1 and mCHERRY-RALF22_{mature} colocalize along the growing dome (scale bar=2.5µm). (C) representative longitudinal optical sections of the shank CW and ROIs showing the presence of overlapping microdomains of demethylesterified HG (PAM1; green) and mCHERRY-RALF22 $_{mature}$ (red) (scale bar=1 μ m). (D) lateral z-projections of the RH shank CW showing the formation of colocalized PAM1 and mCHERRY-RALF22_{mature} circumferential rings (scale bar=5µm). (E) representative longitudinal optical sections of ralf22-2 RHs labeled with PAM1 (demethylesterified HG), 2F4 (Ca²⁺-crosslinked demethylesterified HG) and LM20 (methylesterified HG) (scale bar=10µm). Asterisks indicate expelled intracellular debris as a result of cell bursting. (F) quantification of the labeling intensities for the PAM1 (n_{col-0}=12; n_{PAM1}=16), 2F4 (n_{col-} $_{0}$ =8; n_{2F4} =9) and LM20 epitopes (n_{col-0} =19; n_{PAM1} =9) relative to Col-0 (top barplot), and the ratio between between tip and shank methylesterified HG abundance (LM20; lower barplot). Data is shown as the mean ± SEM. Asterisks represent statistical significance (p-value; **<0.01; ***<0.001). (G) representative longitudinal optical sections of the tip and shank CW of a surviving PAM1 (green)labelled Irx1-1/2-1 RH expressing mCHERRY-RALF22_{mature} (red). Yellow indicates colocalization in the composite frame (scale bar=5µm). (H) Quantification of the PAM1 (green) and mCHERRY-RALF22_{mature} (red) CW labeling intensities in the tip and shank of Irx1-1/2-1 x pRALF22::mCHERRY-RALF22_{mature} and complemented ralf22-2 x pRALF22::mCHERRY-RALF22_{mature} RHs (left half) alongside the tip/shank labeling ratio (right half). Data is shown as the mean ± SEM. Different letters and asterisks represent statistical significance (p-value; ***<0.001). (I) lateral z-projections of the PAM1 labeled lrx1-1/2-1 x pRALF22::mCHERRY-RALF22_{mature} RH shank CW showing the fragmented demethylesterified HG and RALF22 organization (scale bar=5µm).

626 Figure 7. Model of the dual structural and signaling role of RALF22 in the periodic assembly of the 627 root hair cell wall. (A) RALF22, LRX1-RALF22 and methylesterified HG are secreted at the growing RH 628 tip. RALF22 forms a ternary complex with LLG1 and FER, thereby regulating its own secretion and 629 inducing downstream cytosolic calcium signaling and alkalinization of the apical CW. In the CW, 630 Pectin Methyl Esterases (PMEs), which have a high pH optimum, catalyze HG demethylesterification, 631 generating anionic HG through the formation of stretches of negatively charged carboxyl groups. 632 RALF22 and LRX1-RALF22, electrostatically interact with poly-anionic demethylesterified HG. This 633 induces HG dewatering and compaction, and the self-assembly of the HG matrix into (LRX1-)RALF22-634 HG microdomains. (B) These microdomains represent periodic circumferential (LRX1-)RALF22-HG 635 rings which originate in the growing tip, and arise as a consequence of oscillatory (LRX1-)RALF22 636 secretion at the tip and apical pH oscillations which catalyze periodic HG demethylesterification. This 637 temporal periodicity is translated towards the spatial periodicity of (LRX1-)RALF22-HG ring assembly. 638 (LRX1-)RALF22-HG rings illustrate highly anisotropic CW expansion, in which the circumferential 639 strain of the rings greatly surpasses the meridional strain, which is a prerequisite for polar RH 640 growth.

Methods

641

642

657

669

670 671

Plant materials

643 Arabidopsis thaliana ecotype Columbia-0 (Col-0; N1092), ralf22-2 (GK 293H09; N428125; 644 At3g05490), fer-4 (GK 106A06; N69044; At3g51550), eru (SALK 083442; N583442; At5g61350), 645 646 and Ilg1-2 (SALK 086036; N586036; At5g56170) seeds were obtained from the Eurasian 647 Arabidopsis Stock Centre (uNASC). Genotyping of ralf22-2 plants was performed by PCR using T-648 DNA (GTAGATTTCCCGGACATGAAGCCA) and gene-specific primers (FW: 649 ACCGGTCAACCAGTTTCTGCAT, REV: TTCAACGCCTGCACCTAGTGAT). The ralf22-1 line was 650 generated using CRISPR-cas9. Lrx1-1/2-1 (At1g12040, At1g62440) and Irx1-1 x pLRX1::cmyc-LRX1 651 seeds were kindly donated by Prof. Christoph Ringli. Fer-4 x pFER::FER-GFP was kindly donated by Alice Chueng. Col-0 x 35S::GCaMP3 seeds were kindly provided by Prof. Simon Gilroy. ralf22-652 653 1, Col-0 x pEXPa7::G5A, ralf22-2 x pRALF22::mCHERRY-RALF22_{mature}, Irx1-1/2-1 x 654 pRALF22::mCHERRY-RALF22_{mature} and lrx1-1 Х pLRX1::cmyc-LRX1/pRALF22::mCHERRY-655 RALF22_{mature} lines were generated during this study. Eru x pERU::ERU-GFP was generated previously⁴². 656

Growth conditions

658 Seeds were surface sterilized and sown on RH growth medium (3mM KNO₃, 2mM $Ca(NO_3)_2.4H_2O$, 0.5mM MgSO₄.7H₂O, 1mM NH₄H₂PO₄, 1mg.mL-1 thiamine, 0.5 mg.mL-1 659 660 pyridoxine-HCl, 0.5mg.mL-1 nicotinic acid, 0.56mM myo-inositol, 25mM KCl, 17.5mM H₃BO₃, 1mM MnSO₄.H₂O, 1mM ZnSO₄.7H₂O, 0.25mM CuSO₄.5H₂O, 0.25mM (NH₄)6MoO₂₄.4H₂O, 25mM 661 Fe-Na EDTA, 0.8% gelrite or phytagel, 1% sucrose, 2.3mM MES at pH 5.7) for phenotyping or 662 basal Murashige and Skoog (MS) medium (1% sucrose, 1% plant agar, 0.5g.L⁻¹ MES at pH 5.8) 663 664 prior to microfluidic preparation. For live cell imaging and immunolocalization assays, plants were transferred to microfluidic chips and grown overnight in liquid medium (0.1mM KCl, 665 0.1mM CaCl₂, 1mM NaCl, 1% sucrose, 0.5g,L⁻¹ MES at pH 6.0). Imaging of extracellular pH 666 oscillations was performed in unbuffered liquid medium at pH 6.0. 667 668 Seeds were stratified for 2-3 days in the dark at 4°C and plates or microfluidics chips were placed

vertically in a growth chamber with standard growth conditions (16h light-8h dark, 22°C).

Identification of RH-specific RALFs

- Using the BAR ePlant Browser⁷¹, Root-specific transcription was assessed for all *RALFs* that are
- 673 represented on Affymetrix ATH1 arrays. Root-expressed, trichoblast-specific RALFs were
- 674 identified from single cell RNAseq data based on expression in cluster 15 (trichoblasts) in T-SNE
- 675 plots³⁶. For *RALF22*, a trichoblast pseudotime expression profile was generated, showing *RALF22*
- expression in function of the trichoblast's distance to the meristem³⁷.

Immunolocalization

677

691

- Four day old Col-0, ralf22-2, ralf22-2 x pRALF22::mCHERRY-RALF22_{mature}, lrx1-1 x pLRX1::cmyc-
- 679 LRX1/pRALF22::mCHERRY-RALF22_{mature} and Irx1-1/2-1 x pRALF22::mCHERRY-RALF22_{mature}
- seedlings were grown overnight in microfluidics chips⁷² and fixed for 10min in buffered liquid
- 681 medium containing 10% acetic acid and 3.7% formaldehyde. All subsequent steps were
- performed in buffered liquid medium. Each channel was washed (3x5min) and incubated for
- 15min with 50mM NH₄Cl to neutralize residual formaldehyde. After washing (3x5min), aspecific
- 684 binding sites were blocked for 30min in 3% BSA and incubated overnight at 4°C in the presence
- of 3% BSA and a 20-fold (2F4, LM20) or 40-fold (PAM1) primary antibody dilution. Seedlings
- 686 were washed (3% BSA, 3x5min) and incubated for 30min at RT with a 50-fold secondary antibody
- dilution (2F4; goat anti-mouse IgG-FITC, LM20; goat anti-rat IgM-Alexa⁴⁸⁸, PAM1; Rabbit anti-His-
- 688 DyLight⁴⁸⁸, cMyc-LRX1; anti-c-Myc-Alexa⁴⁸⁸). Following a final washing step (3x5min), the chips
- ooo bylight, diviye-lant, and-e-wiye-Alexa j. Following a infal washing step (SXSHIII), the chips
- 689 with labeled seedlings were used for imaging on a Leica TCS SP8 confocal laser scanning
- 690 microscope (Leica-microsystems).

Microscopy

- 692 Six-day-old plants grown on RH growth medium were used for phenotyping. A Nikon AZ100
- 693 multizoom macroscope or Zeiss AxioZoom v16 were used to collect 2h long timelapse
- 694 acquisitions or images of whole roots and individual RHs.
- 695 For fluorescence microscopy plants were grown overnight in uncoated IBIDI μ-slides VI 0.4 filled
- 696 with liquid medium⁷². Each channel contained a single plant.
- 697 Col-0 x pRALF22::GFP plants were counterstained by injecting 10μM propidium iodide (PI) (in
- 698 liquid medium) in each channel. Roots were imaged in xyz-mode using a Leica TCS SP8 confocal
- 699 laser scanning microscope (Leica-microsystems) equipped with a white light laser, 2 HyD
- 700 detectors and a 5x HC PL FLUOTAR dry objective (NA 0.15). GFP (excitation: 488nm, emission:
- 701 501-536nm and PI (excitation: 556, emission: 590-710nm) fluorescence were captured in
- 702 bidirectional line-scanning mode at 8-bit. The z-spacing was set to 1μm-2μm.
- 703 The same system with a 63x HC PL APO CS2 water immersion objective (NA 1.20) was used to
- image [Ca²⁺]_{cyt}, pH_{ext}, growth rate and CW porosity or CW charge dynamics upon treatment with
- 705 RALF22 or EGCG respectively. Col-0 and fer-4 plants were grown in microfluidics chips in 220μL
- of unbuffered liquid medium. Prior to imaging, 160µL of medium was removed from each
- 707 channel. 60μL of medium containing 0.29 mg.mL⁻¹ FITC-110kDa dextran and 0.25 mg.mL⁻¹ TRITC-
- 708 20kDa dextran (for RALF22 treatment) or 0.29 mg.mL⁻¹ FITC-110kDa dextran and 10μM PI (for
- 709 EGCG treatment) was injected back into the channel. Plants were allowed to recover for 30min
- and were subsequently imaged for 10-20min at 30 frames.min⁻¹. FITC/GCaMP3 (excitation:
- 711 488nm, emission: 501-548nm) and TRITC (excitation: 544nm, emission: 560-710nm) or PI
- 712 (excitation: 556nm, emission: 590-710nm) fluorescence were captured using bidirectional line-
- 713 by-line scanning in xyt-mode. After ~4min of steady state growth channels were injected with
- 714 60μL of liquid medium containing either 5μM RALF22 or 100μM EGCG and imaged for another 6-
- 715 16min.
- 716 Timelapse acquisitions of fer-4 x pFER::FER-GFP, eru x pERU::ERU-GFP, ralf22-2 x
- 717 pRALF22::mCHERRY-RALF22_{mature} and lrx1-1/2-1 x pRALF22::mCHERRY-RALF22_{mature} were
- 718 acquired in buffered liquid medium on an inverted Nikon Ti wide-field microsope equipped with
- 719 a micro-lenses enhanced PerkinElmer UltraVIEW Vox spinning disk confocal system and a 60x

- 720 Plan Apo VC oil immersion objective (NA 1.40). GFP (excitation: 488 nm, emission: 525 nm) and
- mCHERRY (excitation: 561 nm, emission: 615 nm) fluorescence were captured for 10-20 min at
- 722 30 frames.min⁻¹.
- 723 The photokinesis unit of the same system was used for Fluorescence Recovery After
- 724 Photobleaching (FRAP) experiments on ralf22-2 x pRALF22::mCHERRY-RALF22_{mature} RHs. To this
- end, growing RHs were imaged for 3-4min after which mCHERRY was bleached in 3 ROIs
- corresponding to the growing tip, the shank just beneath the expanding dome and a region of
- 727 the shank ~100μm below the tip. Recovery of mCHERRY fluorescence was imaged for an
- 728 additional 10min.
- 729 High resolution 3D imaging of mCHERRY-RALF22_{mature} localization in the RH CW was performed
- 730 on a Nikon Ti2 W1-SoRa spinning disk system using the 561 nm laser line, 615 nm emission filter
- 731 and a 100x SR HP Plan Apo silicon immersion objective (NA 1.35). Images were collected in xyz
- 732 mode with a z-spacing of 0.25μm. 3D deconvolution was performed using NIS Elements AR,
- 733 based on a calculated Point Spread Function (PSF) and 10-20 iterations.
- 3D acquisitions of ralf22-2 x pRALF22::mCHERRY-RALF22_{mature} labelled with LM20, 2F4 or PAM1
- 735 antibodies were collected in the same way using the 561 nm and 488 nm laser lines
- 736 respectively.
- 737 Cloning
- 738 The ralf22-1 mutant was generated using CRISPR-cas9 mutagenesis to induce a 182-nucleotide
- 739 deletion downstream of the RALF22 start codon. To this end, two domesticated guide RNA's
- 740 were simultaneously expressed (gRNA1: ATTGGCGATAGTAATCTCAGCCGGTTT; gRNA2:
- 741 ATTgTAGCTACGGTGCTATGAGGGTTT).
- 742 Other constructs were generated by synthesizing the fragment of interest into pDONR221
- 743 (Thermofisher) and subsequent recombination to the desired destination vectors using gateway
- cloning. The pRALF22::GFP transgene was constructed using the entire 2658bp RALF22 promoter
- 745 sequence, including the 5'-UTR. To generate the pRALF22::RALF22 construct, the entire RALF22
- 746 promoter and 360bp genomic sequence including STOP codon were synthesized. The
- 747 pRALF22::mCHERRY-RALF22_{mature} construct was generated by synthesizing the full RALF22
- 748 genomic sequence in which mCHERRY was inserted between the sequences coding for the
- 749 serine-protease cleavage site and the mature RALF22 peptide. To generate a RH-transcribed G5A
- 750 [Ca²⁺]_{cvt} BRET sensor we synthesized a construct containing the 535bp promoter of the
- 751 EXPANSINa7 gene and the G5A sequence⁵⁴. All pDONR221 plasmids were amplified in E. coli.
- 752 Positive colonies were identified by PCR using pRALF22- (FW: TTCTCTGACGCCGTCGACTTTATC,
- 753 REV: GGGTAGCACTATTTCTGCGTTGAC) and GFP-specific (FW: CACATGAAGCAGCACGACT, REV:
- 754 TGCTCAGGTAGTGGTTGTCG) primers. Transgenes were recombined into pFAST-R01 (no tag,
- 755 pOLE1::RFP seed marker), pFAST-R07 (C-terminal GFP, pOLE1::RFP seed marker) or pGWB1 (no
- tag, Kan/hyg resistance) using the gateway LR reaction⁷³. Agrobacterium tumefaciens strain
- 757 LBA4404 transformed with the construct of interest was used to transform Col-0 or ralf22-2
- plants using the floral dip method⁷⁴. To generate the *pRALF22::RALF22*^{R82A,R90A,R100A} construct, the
- 759 full pRALF22 promoter and RALF22 coding sequence (CDS) were amplified from Arabidopsis
- 760 thaliana Col-0 genomic DNA. Structure-based mutations were introduced in the RALF22 CDS by
- site-directed mutagenesis (R82A,R90A,R100A). The transgene was recombined into pGGZ003
- 762 (addgene ID:48869) using GreenGate assembly and subsequently transformed into
- 763 Agrobacterium tumefaciens strain ASE⁷⁵.

Image analysis was performed in Fiji. Root hair length was measured for 7 representative RHs per root, and >20 roots grown on 5 plates.

For *pRALF22::GFP* stacks, the 3D viewer and z-project plugins were used to generate 3D renderings and maximal projections of the acquired z-stacks.

To extract GCaMP3, FITC, TRITC and PI dynamics from timelapse acquisitions, individual frames of the red channel were aligned at subpixel resolution using the template matching plugin and normalized cross correlation as a matching method. The alignment coordinates were used to calculate the subpixel displacement of each frame relative to the first frame, from which the growth rate at each timepoint was calculated. The coordinates were then applied to the corresponding green channel. $[Ca^{2+}]_{cyt}$ traces were extracted from circular ROI in cytoplasm at the tip whereas the pH_{ext} was calculated from the FITC/TRITC ratio extracted from a ROI positioned in the extracellular medium along the expanding dome. The pH_{ext} was calibrated by imaging FITC and TRITC fluorescence in citric acid-sodium phosphate buffered liquid medium, at the exact same imaging settings. A ROI encompassing the apical CW was defined to extract the FITC and TRITC signal corresponding to a change in CW porosity or the PI signal corresponding to changes in CW charge. To quantify changes in cell width, the lateral displacement of the PI-stained CW just beneath the dome was calculated by laterally aligning the CW in a 1 μ m thin ROI (from the center of the cell to the frame's edge). The alignment coordinates were used to calculate the radial expansion of the cell upon EGCG treatment.

To visualize the mobility of mCHERRY-RALF22_{mature} microdomains, we generated kymographs for a linear ROI overlaying the RH CW. To visualize microdomain mobility in the growing RH tip, a kymograph was generated from the apical CW which was straightened in Fiji. The recovery of mCHERRY-RALF22_{mature} fluorescence after bleaching was quantified by extracting the average fluorescence intensity over time in a ROI overlaying the stretch of bleached shank CW. Tip fluorescence recovery was quantified at the very apex after alignment of consecutive frames using the template matching plugin.

To investigate the dynamics of RALF22 secretion, mCHERRY-RALF22_{mature} fluorescence was quantified in a ROI at the very tip of frame aligned timelapse acquisitions, and correlated with the RH growth rate oscillations that were calculated from the alignment coordinates.

RALF22 spacing in the CW was quantified by extracting the mCHERRY-RALF22_{mature} fluorescence intensity pattern from the line pattern present in mCHERRY-RALF22_{mature} kymographs or from a linear ROI drawn along the shank or tip RH CW. The obtained intensity data was detrended in AutoSignal 1.7 (Systat Software) by subtracting a cubic fit. Given that we were interested in the spatial frequency pattern represented by the spacing between individual microdomains, we used Fourier filtering to remove lower frequency oscillation (<0.6Hz) patterns associated with differences in fluorescence intensity along longer stretches of CW. We then generated a continuous wavelet time-frequency spectrum for each trace. The spatial frequency (mCHERRY-RALF22_{mature} fluorescence cycles.μm⁻¹ -power distributions of all RHs were averaged and a gaussian distribution was fitted to get quantitative data on the mCHERRY-RALF22_{mature} microdomain/ring spacing. The ring spacing was calculated as such: ring spacing (μm)= 1 / spatial frequency (mCHERRY-fluorescence cycles.μm⁻¹). Similarly, the predominant period characterizing the oscillatory growth rate pattern was extracted from the power distributions that described the continuous wavelet time-frequency spectrum of the growth rate oscillograms.

Based on the mCHERRY-RALF22_{mature}, 2F4, LM20 and PAM1 Z-stacks, the lateral CW was reconstructed using the 3D project plugin. Colocalization was assessed using the Costes threshold regression method represented in the Coloc2 plugin with 50-100 randomisations⁷⁶.

Calcium assay

To quantify the systemic [Ca²⁺]_{cyt} response in trichoblast cell files upon RALF22 treatment, we generated Col-0 plants expressing the BRET-based GFP-aequorin Ca²⁺indicator G5A⁵⁴ under the

- control of the RH-specific EXPANSINa7 promoter. Col-0 x pEXPa7::G5A plants were grown in 814
- liquid medium in 96-well microplates and incubated overnight in the presence of coelenterazine, 815
- as previously described 54. Following injection of 200nM RALF22_{mature}, RALF22^{R82A,R90A,R100A} or 816
- RALF22 Y75A, Y78A the luminescence was quantified for 20min using a TriStar LB 941 Multimode 817
- 818 microplate reader equipped with automated well-by-well injection (Berthold Technologies). To
- 819 investigate the importance of HG methylesterification, plants were preincubated with 32μM
- EGCG for 30min, 1h, 2h, 3h or overnight prior to RALF22 treatment. The [Ca²⁺]_{cvt} response was 820
- compared between treatments by extracting the area under the curve. 821

Pectin and recombinant protein production

- (AQKKYISYGAMRRNSVPCSRRGASYYNCQRGAQANPYSRGCSTITRCRR), 823 Synthetic RALF22_{mature}
- RALF22^{R82A,R90A,R100A} (AQKKYISYGAMARNSVPCSARGASYYNCQAGAQANPYSRGCSTITRCRR) 824
- RALF22^{Y75A,Y78A} (AQKK<u>A</u>IS<u>A</u>GAMRRNSVPCSRRGASYYNCQRGAQANPYSRGCSTITRCRR) peptides were 825
- 826 chemically synthesized (ProteoGenix, Schiltigheim, France).
- LRX1-RALF22, FER_{ecd}, ERU_{ecd} and LLG1 were produced in insect cells as previously described²⁹. 827
- Codon-optimized synthetic genes for expression in Spodoptera frugiperda (Invitrogen, GeneArt), 828
- 829 coding for Arabidopsis thaliana LLG1 (residues 24-144, At5g56170), ERUecd (residues 28-425,
- 830 At5g61350), FER_{ecd} (residues 1-447, At3g51550), LRX2 (residues 1 to 385; At1g62440), LRX1
- 831 (residues 28-404, At1g12040) and RALF22_{mature} (residues 71-119, At3g05490) domains were
- cloned into a modified pFastBac vector (Geneva Biotech), with a native, 30K⁷⁷ or BIP (native 832
- signal peptide of Drosophila melanogaster) signal peptide; and a TEV (tobacco etch virus 833
- protease) cleavable N- or C-terminal StrepII-9xHis tag. Trichoplusia ni Tnao38 cells^{78,79} were 834
- 835 infected with LLG1, ERULUS, FERONIA or co-infected with LRX1-RALF22 or LRX2-RALF22 with a
- 836 multiplicity of infection (MOI) of 3 and incubated 26 hours at 28°C and 48 hours at 22°C at 110
- rpm. The secreted proteins were purified from the supernatant by sequential Ni²⁺ or Strepll 837
- affinity chromatography. Ni²⁺ (HisTrap excel, Cytiva) and StrepII (Strep-Tactin Superflow high 838
- 839 capacity, IBA Lifesciences) columns were equilibrated in 25mM KPi pH 7.8, 500mM NaCl and
- 25mM Tris pH 8.0, 250mM NaCl, 1mM EDTA respectively. The tags were cleaved with His-tagged 840
- 841 TEV protease at 4°C overnight and removed by a second Ni²⁺ affinity chromatography step.
- Proteins were further purified by SEC on a Superdex 200 Increase 10/300 GL column (Cytiva) 842
- 843 equilibrated in 20mM citrate pH 5.0, 150mM NaCl. Proteins were concentrated using Amicon
- 844 Ultra concentrators (Millipore, molecular weight cut-off 3,000, 10,000 and 30,000), and SDS-
- 845 PAGE was used to assess the purity and integrity of the different proteins.
- 846 High and low methoxyl pectin samples were obtained from CPKelco (Denmark). The degree of
- 847 pectin methylesterification was determined by Fourier transform infrared spectroscopy (FT-IR)
- using an IS50 spectrometer (ThermoFisher Scientific, Courtaboeuf, France). Pectin solutions were 848
- prepared in demineralised water at a concentration of 1 g.L⁻¹, after which the pH was adjusted to 849 pH 6.0, for complete ionization of the carboxylic acid groups. 100µL of solution were put on a 850
- 851 CaF₂ support and dried overnight at 35°C. The IR transmittance was measured at wavenumbers
- 1800 cm⁻¹ to 800 cm⁻¹ at a resolution of 2 cm⁻¹. 200 scans were run per sample and averaged to 852
- obtain mean spectra. The spectra were baseline corrected, and preprocessed (OPUS and
- 853
- The Unscrambler softwares). The ratio (X) of the absorption intensity of the bands around 854
- 1740cm⁻¹ (carbonyl (C = O) stretching) and 1600–1630cm⁻¹ (carboxylate (COO⁻) stretching) was 855
- 856 fitted into a calibration equation (Y = 136.86X + 3.987 to calculate the degree of
- methylesterification $(Y)^{80}$. The analysis was performed in duplicate. 857
- 858 The monosaccharide composition was determined by liquid-gas chromatography. Approx. 5mg
- of pectin powder was hydrolyzed in 2M H₂SO₄ for 2 hours at 100°C in the presence of inositol as 859
- 860 internal standard. Sugars were then reduced, acetylated and analyzed as alditol acetates⁸¹ by
- 861 liquid-gas chromatography (Perkin Elmer, Clarus 580, Shelton, USA) mounted with a DB-225
- 862 fused-silica capillary column (J&W Scientific, Folsorn, CA, USA, at 207°C with H₂ as carrier gas). A

standard solution containing the individual neutral monosaccharides (arabinose, rhamnose, glucose, xylose, galactose and mannose) was treated similarly for calculation of the monosaccharide recovery rates. The analysis was performed in triplicate. The results were expressed as anhydrous sugar to take into account their polysaccharide form in the starting sample. Uronic acids were quantified with the automated colorimetric *m*-hydroxybiphenyl method⁸². The analysis was performed in triplicate.

Molecular interaction assays

We used microscale thermophoresis to identify potential receptor-RALF22 and RALF22-pectin interactions. FER_{ecd}, ERU_{ecd} or LLG1, purified from insect cells, were labeled with the aminereactive dye NT-647 Red-NHS (NanoTemper, Munich, Germany) according to the manufacturer's instructions. Prior to interaction analysis, protein quality was assessed using a Tycho NT.6 (NanoTemper, Munich, Germany). Labeled protein was dissolved in MST buffer (50mM Tris-HCl pH 7.8, 150mM NaCl, 10mM MgCl₂, 0.05% Tween-20). Wild-type or mutant RALF22 was titrated (starting at 100µM) against 20nM of LLG1, FERecd or ERUecd and loaded into premium coated Monolith NT.115 MST capillaries (NanoTemper, Munich, Germany). For the ternary LLG1-RALF22-FER_{ecd} complex, LLG1 (40nM) and wild-type or mutant RALF22 (5μM) were preincubated on ice for 15min and subsequently titrated against 5µM of FER_{ecd}. For RALF22-pectin interactions, wild-type or mutant RALF22 (200µM) was titrated against 40nM Alexa Fluor 647labeled OG7-13⁴⁷. Following 10min incubation at RT, the capillaries were subjected to thermophoresis using a Monolith NT.115 (NanoTemper) at medium MST power and a LED excitation power of 80%. Data were withheld at a S/N >5 and the lack of protein aggregation or ligand-induced initial fluorescence changes. MST data were analyzed using MO. Affinity analysis v2.2.4 NT (NanoTemper).

Quartz Crystal Microbalance with Dissipation Monitoring (QCM-D)

QCM-D was carried out with a "Q-Sense Analyser" (Biolin Scientific, Gothenburg, Sweden) using gold-coated SiO_2 base sensors (QSX 301), spin-coated with 1% polyallylamine hydrochloride (PAH, Sigma-Aldrich, product number 283223) dissolved in water. Using a peristaltic pump a 0.1% pectin solution, in acetate buffer (10mM Na-Acetate pH 5.6, 10mM NaCl), was flown over the PAH layer over the period indicated by the first boxed area in Figs. 3D-F and 5H,I. After a washing step with buffer, protein at a concentration of 1µg/ml (wild-type or mutant RALF22) or $10\mu g/ml$ (LRX2-RALF22), was flown over the pectin layer for the period indicated by the second boxed area in Figs. 3D-F and 5H,I, followed by a washing step. Data presented are frequency (ΔF) and dissipation rate (ΔD) of the 3^{rd} harmonic resonant frequency of the base gold-coated sensors. Before reutilization, sensors were cleaned with a "Piranha" solution (7 vol 95% H₂SO₄ added to 3 vol 30% H₂O₂; respect the order!) using the following protocol: the quartz was incubated (4 in a holder) for 3-5min in Piranha solution. Next, the holder with the quartz was moved to two successive baths with MilliQ water. Then, each quartz was individually rinsed with MilliQ water and dried under a nitrogen stream. If traces still appeared on the surface during drying, rinsing and drying steps were repeated.

Protein structure modelling

The crystal structure of the RALF4 mature peptide (residues 59 to 110; PDB: 6TME)²⁹ was used to build a homology model of the mature RALF22 peptide (residues 71 to 119) through the Swiss-Model homology-modeling server (https://swissmodel.expasy.org/). The docking of LRX2 (PDB:6QXP) and the AlphaFold2 model of LRX1 with the homology model of RALF22 was performed using the Hawdock server⁸³. The N-terminal region of RALF22 (74-88) was docked

into the LLG2 structures (PDB: 6A5E), using the Flexpepdock web-server^{84,85}. The FER receptor was then superimposed according to the crystal structure PDB: 6A5E.

Statistics

Statistics were performed in R^{86} . All data are represented as mean±SEM, and n indicates the number of independent replicates. Significance (α =0.05) was assessed by two-way analysis of variance (ANOVA, parametric) using linear mixed-effects models followed by a TukeyHSD (for pairwise statistical comparison), or by a Kruskal-Wallis test (non-parametric). Normality or deviations thereof were assessed with the Shapiro Wilkinson test (non-normal distribution < W=0.95< normal distribution) and by plotting the corresponding linear model's residual values.

movie legends

919 920

- 921 movie 1. RALF22 loss-of-function root hairs display aberrant growth and frequent bursting.
- Representative 2h timelapse acquisitions of growing Col-0 and *ralf22-2* (-/-) root hairs.
- 923 movie 2. Exogenous RALF22 supplementation induces a FERONIA-dependent growth arrest/signaling
- 924 response and a FERONIA-independent increase in cell wall porosity. Representative longitudinal
- optical section timelapse acquisitions (10min) of growing Col-0 and fer-4 RHs expressing the [Ca²⁺]_{cyt}
- 926 sensor GCaMP3, in the presence of the dextran coupled dyes FITC (110kDa dextran, pH-sensitive) and
- 927 TRITC (20kDa dextran, pH-insensitive). RHs were imaged in a microfluidics chip for 4min prior to
- 928 addition of 5μM RALF22. The RHs response was followed for another 6 min (scale bar=5μm).
- movie3. RALF22 is secreted to the root hair cell wall where it forms immobile periodic microdomains.
- 930 (A) Representative longitudinal optical section timelapse acquisition (10min) of a growing ralf22-2 x
- 931 pRALF22::mCHERRY-RALF22_{mature} RH showing mCHERRY-RALF22_{mature} localization to the entire RH CW.
- 932 Corresponding kymograph showing the immobility of secreted mCHERRY-RALF22mature
- 933 microdomains (shown as vertical red lines) throughout the acquisition (scale bar=5µm). (B) RALF22
- 934 microdomains form in the growing RH dome. Consecutive timelapse frames of the growing tip have
- been aligned to allow visual tracking of mCHERRY-RALF22_{mature} microdomains as they move from tip
- to shank as the tip grows forward. The concave shape of the growing dome was straightened to
- generate a kymograph. Red lines in the kymograph depict mCHERRY-RALF22_{mature} microdomains,
- 938 which originate at the very apex and remain immobile as they move towards the shank (scale
- 939 bar=5μm).
- 940 movie 4. RALF22 is secreted at the growing root hair tip. Representative longitudinal optical section
- 941 timelapse acquisition (10 min) of a growing ralf22-2 x pRALF22::mCHERRY-RALF22_{mature} RH. After
- 4min of steady state growth, mCHERRY-RALF22mature fluorescence was bleached in a ROI in the tip
- and shank. Fluorescence Recovery After Photobleaching was followed for an additional 6min. Rapid
- 944 mCHERRY-RALF22_{mature} fluorescence recovery was observed in the tip, but not in subapical regions
- 945 (scale bar=5μm).
- 946 movie 5. The *lrx1-1/2-1* root hair phenotype is indistinguishable from *ralf22-2*. Representative 2h
- timelapse acquisitions of growing Col-0, ralf22-2 and lrx1-1/2-1 RHs.
- 948 movie 6. Pectin demethylesterification is crucial for root hair growth. Representative longitudinal
- optical section timelapse acquisitions (10 min) of growing Col-0 RHs expressing the [Ca²⁺]_{cvt} sensor
- 950 GCaMP3 in the of dextran coupled FITC (110kDa dextran, pH-sensitive) and propidium iodide (CW
- charge reporter). Steady state RH growth was imaged for 4min prior to treatment with the Pectin
- 952 Methylesterase (PME) inhibitor EGCG (100μM) or growth medium (mock). The RH's response was
- 953 followed for an additional 6min.
- movie 7. LRX1/2 is required for RALF22 secretion. Representative longitudinal optical section
- 955 timelapse acquisitions (10min) of growing ralf22-2 x pRALF22::mCHERRY-RALF22_{mature} and lrx1-1/2-1 x
- 956 pRALF22::mCHERRY-RALF22_{mature} RHs illustrating the accumulation of mCHERRY-RALF22_{mature} in
- 957 intracellular compartments in *lrx1-1/2-1* RHs.

References

- 959 1. Kjellén, L., & Lindahl, U. (2018). Specificity of glycosaminoglycan-protein interactions. 960 Current Opinion in Structural Biology, 50, 101–108.
- 961 https://doi.org/10.1016/j.sbi.2017.12.011

962 2. Haas, K. T., Wightman, R., Peaucelle, A., & Höfte, H. (2021). The role of pectin phase 963 separation in plant cell wall assembly and growth. The Cell Surface, 7, 100054. 964 https://doi.org/10.1016/j.tcsw.2021.100054

- 3. Coen, E., & Cosgrove, D. J. (2023). The mechanics of plant morphogenesis. Science (New York, N.Y.), 379(452), eade8055. https://doi.org/10.1126/science.ade8055
- 967 4. Wilson, L. A., Deligey, F., Wang, T., & Cosgrove, D. J. (2021). Saccharide analysis of onion 968 outer epidermal walls. Biotechnology for Biofuels, 14(1), 1–14. 969 https://doi.org/10.1186/s13068-021-01923-z
 - 5. Levesque-Tremblay, G., Pelloux, J., Braybrook, S. A., & Müller, K. (2015). Tuning of pectin methylesterification: consequences for cell wall biomechanics and development. Planta, 242(4), 791–811. https://doi.org/10.1007/s00425-015-2358-5
 - 6. Vincent, R. R., & Williams, M. A. K. (2009). Microrheological investigations give insights into the microstructure and functionality of pectin gels. Carbohydrate Research, 344(14), 1863–1871. https://doi.org/10.1016/j.carres.2008.11.021
 - 7. Derbyshire, P., McCann, M. C., & Roberts, K. (2007). Restricted cell elongation in *Arabidopsis* hypocotyls is associated with a reduced average pectin esterification level. BMC Plant Biology, 7(31), 1–12. https://doi.org/10.1186/1471-2229-7-31
 - 8. Boyer, J. S. (2016). Enzyme-less growth in *chara* and terrestrial plants. Frontiers in Plant Science, 7(June), 1–15. https://doi.org/10.3389/fpls.2016.00866
 - 9. Rojas, E. R., Hotton, S., & Dumais, J. (2011). Chemically mediated mechanical expansion of the pollen tube cell wall. Biophysical Journal, 101(8), 1844–1853. https://doi.org/10.1016/j.bpj.2011.08.016
 - 10. Dumais, J. (2021). Mechanics and hydraulics of pollen tube growth. New Phytologist, 232(4), 1549–1565. https://doi.org/10.1111/nph.17722
 - 11. Haas, K. T., Wightman, R., Meyerowitz, E. M., & Peaucelle, A. (2020). Pectin homogalacturonan nanofilament expansion drives morphogenesis in plant epidermal cells. Science, 367(6481), 1003–1007. https://doi.org/10.1126/science.aaz5103
 - 12. Ma, Y., Jonsson, K., Aryal, B., De Veylder, L., Hamant, O., & Bhalerao, R. P. (2022). Endoreplication mediates cell size control via mechanochemical signaling from cell wall. Science Advances, 8(49), 1–11. https://doi.org/10.1126/sciadv.abq2047
 - 13. Bidhendi, A. J., & Geitmann, A. (2016). Relating the mechanics of the primary plant cell wall to morphogenesis. Journal of Experimental Botany, 67(2), 449–461. https://doi.org/10.1093/jxb/erv535
 - 14. Geitmann, A., & Ortega, J. K. E. (2009). Mechanics and modeling of plant cell growth. Trends in Plant Science, 14(9), 467–478. https://doi.org/10.1016/j.tplants.2009.07.006
 - 15. Palin, R., & Geitmann, A. (2012). The role of pectin in plant morphogenesis. BioSystems, 109(3), 397–402. https://doi.org/10.1016/j.biosystems.2012.04.006
 - 16. Richter, R. P., Baranova, N. S., Day, A. J., & Kwok, J. C. (2018). Glycosaminoglycans in extracellular matrix organisation: are concepts from soft matter physics key to understanding the formation of perineuronal nets? Current Opinion in Structural Biology, 50, 65–74. https://doi.org/10.1016/j.sbi.2017.12.002
 - 17. Valentin, R., Cerclier, C., Geneix, N., Aguié-Béghin, V., Gaillard, C., Ralet, M. C., & Cathala, B. (2010). Elaboration of extensin-pectin thin film model of primary plant cell wall. Langmuir, 26(12), 9891–9898. https://doi.org/10.1021/la100265d
 - 18. Fry, S. C. (1982). Isodityrosine, a new cross-linking amino acid from plant cell-wall glycoprotein. The Biochemical Journal, 204(2), 449–455. https://doi.org/10.1042/bj2040449 Brady, J. D., Sadler, I. H., & Fry, S. C. (1996). Di-isodityrosine, a novel tetrameric derivative of tyrosine in plant cell wall proteins: A new potential cross-link. Biochemical Journal, 315(1), 323–327. https://doi.org/10.1042/bj3150323
- 1011 19. Held, M. A., Tan, L., Kamyabi, A., Hare, M., Shpak, E., & Kieliszewski, M. J. (2004). Di-1012 isodityrosine is the intermolecular cross-link of isodityrosine-rich extensin analogs cross-

1013 linked in vitro. Journal of Biological Chemistry, 279(53), 55474–55482. 1014 https://doi.org/10.1074/jbc.M408396200

- 20. Moussu, S., & Ingram, G. (2023). The EXTENSIN enigma. The Cell Surface, 9, 100094.
 https://doi.org/10.1016/j.tcsw.2023.100094
 - 21. Pearce, G., Moura, D. S., Stratmann, J., & Ryan, C. A. (2001). RALF, a 5-kDa ubiquitous polypeptide in plants, arrests root growth and development. Proceedings of the National Academy of Sciences of the United States of America, 98(22), 12843–12847. https://doi.org/10.1073/pnas.201416998
 - 22. Abarca, A., Franck, C. M., & Zipfel, C. (2021). Family-wide evaluation of rapid alkalinization factor peptides. Plant Physiology, 187(2), 996–1010. https://doi.org/10.1093/plphys/kiab308
 - 23. Xiao, Y., Stegmann, M., Han, Z., DeFalco, T. A., Parys, K., Xu, L., Belkhadir, Y., Zipfel, C., & Chai, J. (2019). Mechanisms of RALF peptide perception by a heterotypic receptor complex. Nature, 572(7768), 270–274. https://doi.org/10.1038/s41586-019-1409-7
 - 24. Ge, Z., Bergonci, T., Zhao, Y., Zou, Y., Du, S., Liu, M.-C., Luo, X., Ruan, H., Garcia-Valencia, L. E., Zhong, S., Hou, S., Huang, Q., Lai, L., Moura, D. S., Gu, H., Dong, J., Wu, H.-M., Dresselhaus, T., Xiao, J., ... Qu, L.-J. (2017). *Arabidopsis* pollen tube integrity and sperm release are regulated by RALF-mediated signaling. Science, 358(December), 1596–1600. https://doi.org/10.1126/science.aao3642
 - 25. Ge, Z., Zhao, Y., Liu, M. C., Zhou, L. Z., Wang, L., Zhong, S., Hou, S., Jiang, J., Liu, T., Huang, Q., Xiao, J., Gu, H., Wu, H. M., Dong, J., Dresselhaus, T., Cheung, A. Y., & Qu, L. J. (2019). LLG2/3 Are Co-receptors in BUPS/ANX-RALF Signaling to Regulate *Arabidopsis* Pollen Tube Integrity. Current Biology, 29(19), 3256-3265.e5. https://doi.org/10.1016/j.cub.2019.08.032
 - 26. Gao, Q., Wang, C., Xi, Y., Shao, Q., Hou, C., Li, L., & Luan, S. (2023). RALF signaling pathway activates MLO calcium channels to maintain pollen tube integrity. Cell Research, 33(1), 71–79. https://doi.org/10.1038/s41422-022-00754-3
 - 27. Mecchia, M. A., Santos-Fernandez, G., Duss, N. N., Somoza, S. C., Boisson-Dernier, A., Gagliardini, V., Martínez-Bernardini, A., Fabrice, T. N., Ringli, C., Muschietti, J. P., & Grossniklaus, U. (2017). RALF4/19 peptides interact with LRX proteins to control pollen tube growth in *Arabidopsis*. Science, 358(6370), 1600–1603. https://doi.org/10.1126/science.aao5467
 - 28. Solis-Miranda, J., & Quinto, C. (2021). The CrRLK1L subfamily: One of the keys to versatility in plants. Plant Physiology and Biochemistry, 166(May), 88–102. https://doi.org/10.1016/j.plaphy.2021.05.028
 - 29. Moussu, S., Broyart, C., Santos-Fernandez, G., Augustin, S., Wehrle, S., Grossniklaus, U., & Santiago, J. (2020). Structural basis for recognition of RALF peptides by LRX proteins during pollen tube growth. Proceedings of the National Academy of Sciences of the United States of America, 117(13), 7494–7503. https://doi.org/10.1073/pnas.2000100117
 - 30. Herger, A., Gupta, S., Kadler, G., Franck, C. M., Boisson-Dernier, A., & Ringli, C. (2020). Overlapping functions and protein-protein interactions of LRR-extensins in *Arabidopsis*. PLoS Genetics, 16(6), 1–24. https://doi.org/10.1371/journal.pgen.1008847
 - 31. Zhao, C., Zayed, O., Yu, Z., Jiang, W., Zhu, P., Hsu, C. C., Zhang, L., Andy Tao, W., Lozano-Durán, R., & Zhu, J. K. (2018). Leucine-rich repeat extensin proteins regulate plant salt tolerance in *Arabidopsis*. Proceedings of the National Academy of Sciences of the United States of America, 115(51), 13123–13128. https://doi.org/10.1073/pnas.1816991115
 - 32. Baumberger, N., Doesseger, B., Guyot, R., Diet, A., Parsons, R. L., Clark, M. A., Simmons, M. P., Bedinger, P., Goff, S. A., Ringli, C., & Keller, B. (2003). Whole-genome comparison of leucine-rich repeat extensins in *Arabidopsis* and rice. A conserved family of cell wall proteins form a vegetative and a reproductive clade. Plant Physiology, 131(3), 1313–1326. https://doi.org/10.1104/pp.102.014928
- 33. Schoenaers, S., Balcerowicz, D., & Vissenberg, K. (2017). Molecular Mechanisms Regulating Root Hair Tip Growth: A Comparison with Pollen Tubes. In Pollen Tip Growth: From

- 1064 Biophysical Aspects to Systems Biology (pp. 167–243). Springer. https://doi.org/10.1007/978-1065 3-319-56645-0 9
- 34. Hocq, L., Pelloux, J., & Lefebvre, V. (2017). Connecting Homogalacturonan-Type Pectin Remodeling to Acid Growth. Trends in Plant Science, 22(1), 20–29. https://doi.org/ 1068 10.1016/j.tplants.2016.10.009

1071

1072

1073

1074

1075

1076

1077

1078

1079

1080

1081 1082

1083

1084

1085

1086

1087 1088

1089

1090

1091 1092

1093 1094

1095

1096

1097

1098 1099

1100 1101

1102

1103

1104

1105

- 35. Pacifici, E., Di Mambro, R., Dello Ioio, R., Costantino, P., & Sabatini, S. (2018). Acidic cell elongation drives cell differentiation in the *Arabidopsis* root. The EMBO Journal, 37(16), 1–9. https://doi.org/10.15252/embj.201899134
- 36. Denyer, T., Ma, X., Klesen, S., Scacchi, E., Nieselt, K., & Timmermans, M. C. P. (2019). Spatiotemporal Developmental Trajectories in the *Arabidopsis* Root Revealed Using High-Throughput Single-Cell RNA Sequencing. Developmental Cell, 48(6), 840-852.e5. https://doi.org/10.1016/j.devcel.2019.02.022
 - 37. Stegmann, M., Monaghan, J., Smakowska-Luzan, E., Rovenich, H., Lehner, A., Holton, N., Belkhadir, Y., & Zipfel, C. (2017). The receptor kinase FER is a RALF-regulated scaffold controlling plant immune signaling. Science, 355(6322), 287–289. https://doi.org/10.1126/science.aal2541
 - 38. Gonneau, M., Desprez, T., Martin, M., Doblas, V. G., Bacete, L., Miart, F., Sormani, R., Hématy, K., Renou, J., Landrein, B., Murphy, E., Van De Cotte, B., Vernhettes, S., De Smet, I., & Höfte, H. (2018). Receptor Kinase THESEUS1 Is a Rapid Alkalinization Factor 34 Receptor in *Arabidopsis*. Current Biology, 2452–2458. https://doi.org/10.1016/j.cub.2018.05.075
 - 39. Srivastava, R., Liu, J. X., Guo, H., Yin, Y., & Howell, S. H. (2009). Regulation and processing of a plant peptide hormone, AtRALF23, in *Arabidopsis*. Plant Journal, 59(6), 930–939. https://doi.org/10.1111/j.1365-313X.2009.03926.x
 - 40. Zhao, C., Zayed, O., Yu, Z., Jiang, W., Zhu, P., Hsu, C. C., Zhang, L., Andy Tao, W., Lozano-Durán, R., & Zhu, J. K. (2018). Leucine-rich repeat extensin proteins regulate plant salt tolerance in *Arabidopsis*. Proceedings of the National Academy of Sciences of the United States of America, 115(51), 13123–13128. https://doi.org/10.1073/pnas.1816991115
 - 41. Schoenaers, S., Balcerowicz, D., Breen, G., Hill, K., Zdanio, M., Mouille, G., Holman, T. J., Oh, J., Wilson, M. H., Nikonorova, N., Vu, L. D., De Smet, I., Swarup, R., De Vos, W. H., Pintelon, I., Adriaensen, D., Grierson, C., Bennett, M. J., & Vissenberg, K. (2018). The Auxin-Regulated CrRLK1L Kinase ERULUS Controls Cell Wall Composition during Root Hair Tip Growth. Current Biology, 28(5), 722-732.e6. https://doi.org/10.1016/j.cub.2018.01.050
 - 42. Duan, Q., Kita, D., Li, C., Cheung, A. Y., & Wu, H. M. (2010). FERONIA receptor-like kinase regulates RHO GTPase signaling of root hair development. Proceedings of the National Academy of Sciences of the United States of America, 107(41), 17821–17826. https://doi.org/10.1073/pnas.1005366107
 - 43. Shen, Q., Bourdais, G., Pan, H., Robatzek, S., & Tang, Di. (2017). *Arabidopsis* glycosylphosphatidylinositol-anchored protein LLG1 associates with and modulates FLS2 to regulate innate immunity. Proceedings of the National Academy of Sciences of the United States of America, 114(22), 5749–5754. https://doi.org/10.1073/pnas.1614468114
- 44. Toyota, M., Spencer, D., Sawai-toyota, S., Jiaqi, W., Zhang, T., Koo, A. J., Howe, G. A., & Gilroy, S. (2018). Glutamate triggers long-distance, calcium-based plant defense signaling. Science, 361(September), 1112–1115. https://doi.org/10.1126/science.aat7744
- 45. Voetmann, L. M., Rolin, B., Kirk, R. K., Pyke, C., & Hansen, A. K. (2023). The intestinal permeability marker FITC-dextran 4kDa should be dosed according to lean body mass in obese mice. Nutrition and Diabetes, 13(1), 4–8. https://doi.org/10.1038/s41387-022-00230-2
- 1110 46. Chen, H., Liu, Y.-C., Zhang, Z., Li, M., Du, L., Wu, P.-C., Chong, W.-H., Ren, F., Zheng, W., & Liu, T.-M. (2022). Mouse Strain- and Charge-Dependent Vessel Permeability of Nanoparticles at 1111 1112 the Lower Size Limit. Frontiers in Chemistry, 10(July), 1-9. 1113 https://doi.org/10.3389/fchem.2022.944556
- 47. Mravec, J., Kračun, S. K., Rydahl, M. G., Westereng, B., Pontiggia, D., De Lorenzo, G., Domozych, D. S., & Willats, W. G. T. (2017). An oligogalacturonide-derived molecular probe

- demonstrates the dynamics of calcium-mediated pectin complexation in cell walls of tipgrowing structures. Plant Journal, 91(3), 534–546. https://doi.org/10.1111/tpj.13574
- 48. Jaafar, Z., Mazeau, K., Boissière, A., Le Gall, S., Villares, A., Vigouroux, J., Beury, N., Moreau, C., Lahaye, M., & Cathala, B. (2019). Meaning of xylan acetylation on xylan-cellulose interactions: A quartz crystal microbalance with dissipation (QCM-D) and molecular dynamic study. Carbohydrate Polymers, 226(September), 115315. https://doi.org/10.1016/j.carbpol.2019.115315
- 49. Tanaka, T. (1981). Gels. Scientific American, 124–138.
 https://doi.org/10.1038/scientificamerican0181-124

1126

1127

1128

1129

1130

1131

1132

1133

1134

1135

11361137

1138

1139

11401141

1142

11431144

11451146

1147

1148

1149

1150

1151

1152

1153

1154

1155

1156

1157

- 50. Shibayama, M., & Tanaka, T. (1993). Volume phase transition and related phenomena of polymer gels. Advances in Polymer Science, 109, 1–60. https://doi.org/10.1007/3-540-56791-7 1
 - 51. Baumberger, N., Steiner, M., Ryser, U., Keller, B., & Ringli, C. (2003). Synergistic interaction of the two paralogous *Arabidopsis* genes LRX1 and LRX2 in cell wall formation during root hair development. Plant Journal, 35(1), 71–81. https://doi.org/10.1046/j.1365-313X.2003.01784.x
- 52. Baumberger, N., Ringli, C., & Keller, B. (2001). The chimeric leucine-rich repeat/extensin cell wall protein LRX1 is required for root hair morphogenesis in *Arabidopsis thaliana*. Genes and Development, 15(9), 1128–1139. https://doi.org/10.1101/gad.200201
- 53. Rounds, C. M., Lubeck, E., Hepler, P. K., & Winship, L. J. (2011). Propidium iodide competes with Ca²⁺ to label pectin in pollen tubes and *Arabidopsis* root hairs. Plant Physiology, 157(1), 175–187. https://doi.org/10.1104/pp.111.182196
- 54. Xiong, T. C., Ronzier, E., Sanchez, F., Corratgé-Faillie, C., Mazars, C., & Thibaud, J. B. (2014). Imaging long distance propagating calcium signals in intact plant leaves with the BRET-based GFP-aequorin reporter. Frontiers in Plant Science, 5(43), 1–13. https://doi.org/10.3389/fpls.2014.00043
- 55. Xu, F., Gonneau, M., Faucher, E., Habrylo, O., Lefebvre, V., Domon, J. M., Martin, M., Sénéchal, F., Peaucelle, A., Pelloux, J., & Höfte, H. (2022). Biochemical characterization of Pectin Methylesterase Inhibitor 3 from *Arabidopsis thaliana*. The Cell Surface, 8(July), 4–11. https://doi.org/10.1016/j.tcsw.2022.100080
- 56. Verhertbruggen, Y., Marcus, S. E., Haeger, A., Ordaz-Ortiz, J. J., & Knox, J. P. (2009). An extended set of monoclonal antibodies to pectic homogalacturonan. Carbohydrate Research, 344(14), 1858–1862. https://doi.org/10.1016/j.carres.2008.11.010
- 57. Liners, F., Letesson, J. J., Didembourg, C., & Van Cutsem, P. (1989). Monoclonal Antibodies against Pectin: Recognition of a Conformation Induced by Calcium. Plant Physiology, 91(4), 1419–1424. https://doi.org/10.1104/pp.91.4.1419
- 58. Willats, W. G. T., Gilmartin, P. M., Mikkelsen, J. D., & Knox, J. P. (1999). Cell wall antibodies without immunization: Generation and use of de-esterified homogalacturonan block-specific antibodies from a naive phage display library. Plant Journal, 18(1), 57–65. https://doi.org/10.1046/j.1365-313X.1999.00427.x
 - 59. Langford-Smith, A., Keenan, T. D. L., Clark, S. J., Bishop, P. N., & Day, A. J. (2014). The role of complement in age-related macular degeneration: Heparan sulphate, a ZIP code for complement factor H? Journal of Innate Immunity, 6(4), 407–416. https://doi.org/10.1159/000356513
- 1159 60. Voxeur, A., Habrylo, O., Guénin, S., Miart, F., Soulié, M. C., Rihouey, C., Pau-Roblot, C., Domon, J. M., Gutierrez, L., Pelloux, J., Mouille, G., Fagard, M., Höfte, H., & Vernhettes, S. (2019). Oligogalacturonide production upon *Arabidopsis thaliana-Botrytis cinerea* interaction. Proceedings of the National Academy of Sciences of the United States of America, 116(39), 19743–19752. https://doi.org/10.1073/pnas.1900317116
- 1164 61. Willats, W. G. T., McCartney, L., Steele-King, C. G., Marcus, S. E., Mort, A., Huisman, M., Van 1165 Alebeek, G. J., Schols, H. A., Voragen, A. G. J., Le Goff, A., Bonnin, E., Thibault, J. F., & Knox, J. 1166 P. (2004). A xylogalacturonan epitope is specifically associated with plant cell detachment. 1167 Planta, 218(4), 673–681. https://doi.org/10.1007/s00425-003-1147-8

- 1168 62. Tanaka, T., Annaka, M., Ilmain, F., Ishii, K., Kokufuta, E., Suzuki, A., & Tokita, M. (1992). Phase 1169 Transitions of Gels. In NATO ASI Series, Vol. 64. Mechanics of Swelling (pp. 683–703). 1170 https://doi.org/10.1146/ANNUREV.MS.22.080192.001331
- 1171 63. Cannon, M. C., Terneus, K., Hall, Q., Tan, L., Wang, Y., Wegenhart, B. L., Chen, L., Lamport, D.
 1172 T. A., Chen, Y., & Kieliszewski, M. J. (2008). Self-assembly of the plant cell wall requires an
 1173 extensin scaffold. Proceedings of the National Academy of Sciences of the United States of
 1174 America, 105(6), 2226–2231. https://doi.org/10.1073/pnas.0711980105

- 64. Shih, H. W., Miller, N. D., Dai, C., Spalding, E. P., & Monshausen, G. B. (2014). The receptor-like kinase FERONIA is required for mechanical signal transduction in *Arabidopsis* seedlings. Current Biology, 24(16), 1887–1892. https://doi.org/10.1016/j.cub.2014.06.064
- 65. Tang, W., Lin, W., Zhou, X., Guo, J., Dang, X., Li, B., Lin, D., & Yang, Z. (2022). Mechanotransduction via the pectin-FERONIA complex activates ROP6 GTPase signaling in *Arabidopsis* pavement cell morphogenesis. Current Biology, 32(3), 508-517.e3. https://doi.org/10.1016/j.cub.2021.11.031
 - 66. Feng, W., Kita, D., Peaucelle, A., Cartwright, H. N., Doan, V., Duan, Q., Liu, M. C., Maman, J., Steinhorst, L., Schmitz-Thom, I., Yvon, R., Kudla, J., Wu, H. M., Cheung, A. Y., & Dinneny, J. R. (2018). The FERONIA Receptor Kinase Maintains Cell-Wall Integrity during Salt Stress through Ca²⁺ Signaling. Current Biology, 28(5), 666-675.e5. https://doi.org/10.1016/j.cub.2018.01.023
 - 67. Brost, C., Studtrucker, T., Reimann, R., Denninger, P., Czekalla, J., Krebs, M., Fabry, B., Schumacher, K., Grossmann, G., & Dietrich, P. (2019). Multiple cyclic nucleotide-gated channels coordinate calcium oscillations and polar growth of root hairs. Plant Journal, 99(5), 910–923. https://doi.org/10.1111/tpj.14371
 - 68. Park, S., Szumlanski, A. L., Gu, F., Guo, F., & Nielsen, E. (2011). A role for CSLD3 during cell-wall synthesis in apical plasma membranes of tip-growing root-hair cells. Nature Cell Biology, 13, 973–980.
- 69. Cavalier, D. M., Lerouxel, O., Neumetzler, L., Yamauchi, K., Reinecke, A., Freshour, G., Zabotina, O. A., Hahn, M. G., Burgert, I., Pauly, M., Raikhel, N. V., & Keegstra, K. (2008). Disrupting two *Arabidopsis thaliana* xylosyltransferase genes results in plants deficient in xyloglucan, a major primary cell wall component. Plant Cell, 20(6), 1519–1537. https://doi.org/10.1105/tpc.108.059873
- 70. Lin, C., Choi, H.-S., & Cho, H.-T. (2011). Root hair-specific EXPANSIN A7 is required for root hair elongation in *Arabidopsis*. Molecules and Cells, 31, 393–397. https://doi.org/10.1007/s10059-011-0046-2
- 71. Winter, D., Vinegar, B., Nahal, H., Ammar, R., Wilson, G. V., & Provart, N. J. (2007). An "electronic fluorescent pictograph" Browser for exploring and analyzing large-scale biological data sets. PLoS ONE, 2(8), 1–12. https://doi.org/10.1371/journal.pone.0000718
- 72. Herburger, K., Schoenaers, S., Vissenberg, K., & Mravec, J. (2022). Shank-localized cell wall growth contributes to *Arabidopsis* root hair elongation. Nature Plants, 8(11), 1222–1232. https://doi.org/10.1038/s41477-022-01259-y
 - 73. Shimada, T. L., Shimada, T., & Hara-Nishimura, I. (2010). A rapid and non-destructive screenable marker, FAST, for identifying transformed seeds of *Arabidopsis thaliana*: TECHNICAL ADVANCE. Plant Journal, 61(3), 519–528. https://doi.org/10.1111/j.1365-313X.2009.04060.x
- 74. Clough, S. J., & Bent, A. F. (1998). Floral dip: A simplified method for *Agrobacterium*-mediated transformation of *Arabidopsis thaliana*. Plant Journal, 16(6), 735–743. https://doi.org/10.1046/j.1365-313X.1998.00343.x
- 1214 75. Lampropoulos, A., Sutikovic, Z., Wenzl, C., Maegele, I., Lohmann, J. U., & Forner, J. (2013).
 1215 GreenGate A novel, versatile, and efficient cloning system for plant transgenesis. PLoS ONE,
 1216 8(12). https://doi.org/10.1371/journal.pone.0083043
- 76. Costes, S. V., Daelemans, D., Cho, E. H., Dobbin, Z., Pavlakis, G., & Lockett, S. (2004).

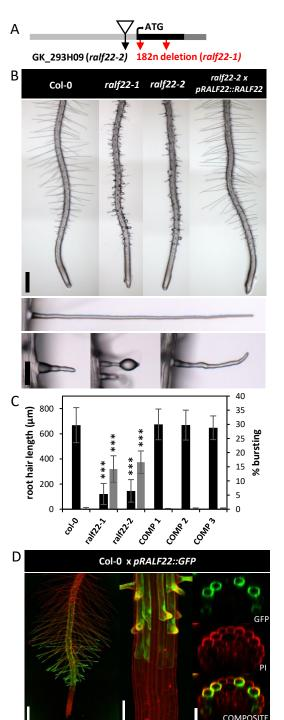
 Automatic and quantitative measurement of protein-protein colocalization in live cells.

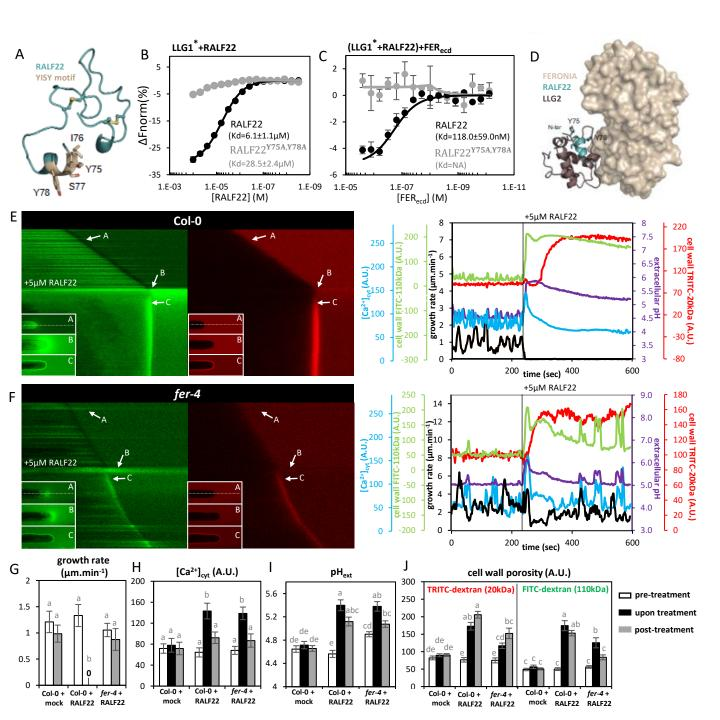
 Biophysical Journal, 86(6), 3993–4003. https://doi.org/10.1529/biophysj.103.038422

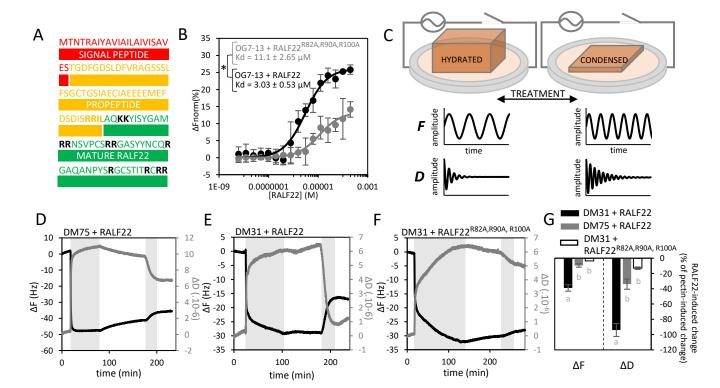
77. Futatsumori-Sugai, M., & Tsumoto, K. (2010). Signal peptide design for improving recombinant protein secretion in the *Baculovirus* expression vector system. Biochemical and Biophysical Research Communications, 391(1), 931–935. https://doi.org/10.1016/j.bbrc.2009.11.167

- 78. Hashimoto, Y., Zhang, S., & Blissard, G. W. (2010). Ao38, a new cell line from eggs of the black witch moth, *Ascalapha odorata* (Lepidoptera: *Noctuidae*), is permissive for AcMNPV infection and produces high levels of recombinant proteins. BMC Biotechnology, 10(50). https://doi.org/10.1186/1472-6750-10-50
 - 79. Hashimoto, Y., Zhang, S., Zhang, S., Chen, Y. R., & Blissard, G. W. (2012). Correction: BTI-Tnao38, a new cell line derived from *Trichoplusia ni*, is permissive for AcMNPV infection and produces high levels of recombinant proteins. BMC Biotechnology, 12, 3–6. https://doi.org/10.1186/1472-6750-12-12
 - 80. Kyomugasho, C., Christiaens, S., Shpigelman, A., Van Loey, A. M., & Hendrickx, M. E. (2015). FT-IR spectroscopy, a reliable method for routine analysis of the degree of methylesterification of pectin in different fruit- and vegetable-based matrices. Food Chemistry, 176, 82–90. https://doi.org/10.1016/j.foodchem.2014.12.033
 - 81. Englyst, H., Wiggins, H. S., & Cummings, J. H. (1982). Determination of the non-starch polysaccharides in plant foods by gas Liquid chromatography of constituent sugars as alditol acetates. The Analyst, 107(1272), 307–318. https://doi.org/10.1039/AN9820700307
 - 82. Thibault, J.-F. (1979). Automatisation du dosage des substances pectiques par la méthode au méta-hidroxydiphenyl. Lebensmittel-Wissenschaft Und Technologie, 12(5), 247–251.
 - 83. Weng, G., Wang, E., Wang, Z., Liu, H., Zhu, F., Li, D., & Hou, T. (2019). HawkDock: a web server to predict and analyze the protein-protein complex based on computational docking and MM/GBSA. Nucleic Acids Research, 47(W1), W322–W330. https://doi.org/10.1093/nar/gkz397
 - 84. Raveh, B., London, N., & Schueler-Furman, O. (2010). Sub-angstrom modeling of complexes between flexible peptides and globular proteins. Proteins: Structure, Function and Bioinformatics, 78(9), 2029–2040. https://doi.org/10.1002/prot.22716
 - 85. London, N., Raveh, B., Cohen, E., Fathi, G., & Schueler-Furman, O. (2011). Rosetta FlexPepDock web server High resolution modeling of peptide-protein interactions. Nucleic Acids Research, 39(SUPPL. 2), 249–253. https://doi.org/10.1093/nar/gkr431
- 1251 86. Team, R. C. (2021). R: A language and environment for statistical computing. R Foundation for Statistical Computing, Vienna, Austria. https://www.r-project.org/

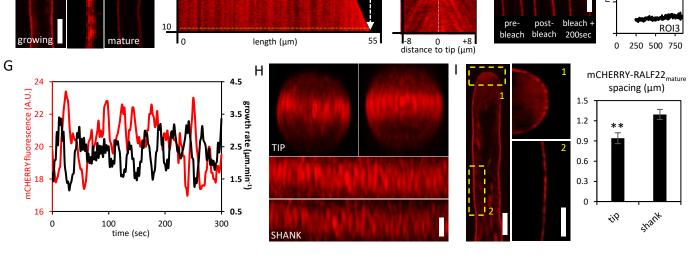
(which was not certified by peer review) is the author/funder. All rights reserved. No reuse allowed without permission.

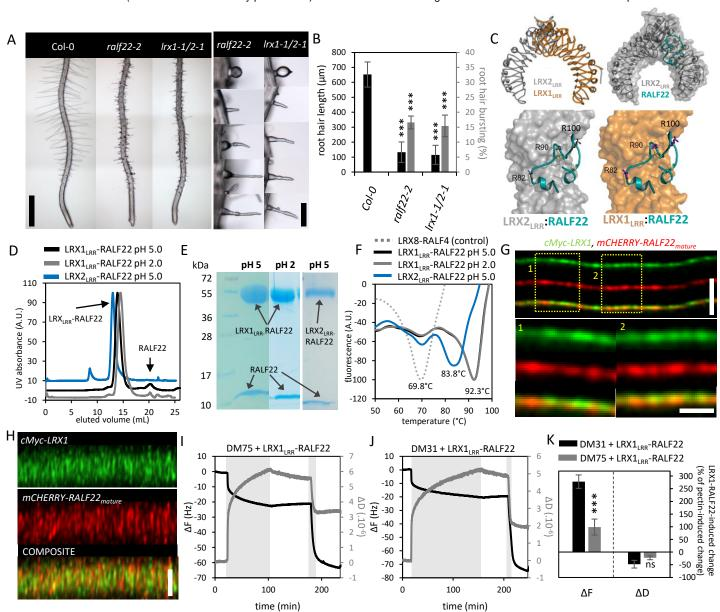


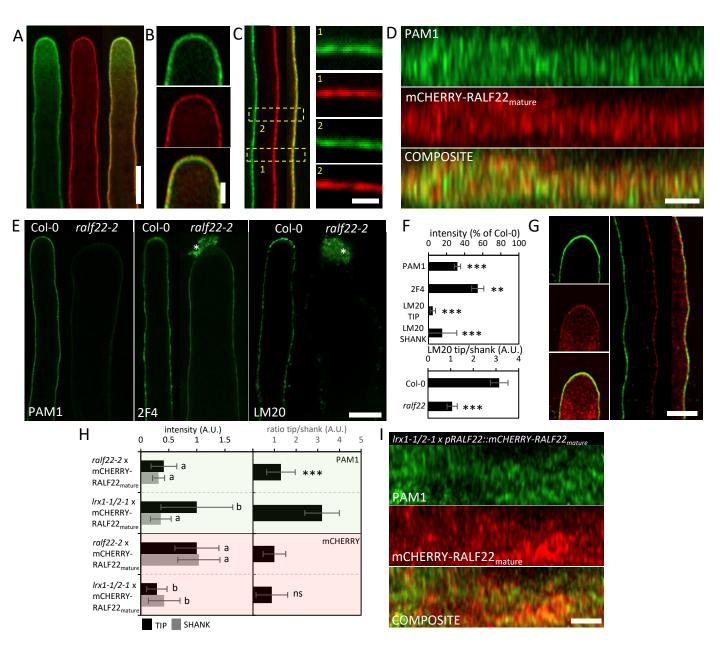




C







(which was not certified by peer review) is the author/funder. All rights reserved. No reuse allowed without permission.

